Title

How to sustain a CO2-thermosiphon in a partially saturated geothermal reservoir: Lessons learned from field experiment and numerical modeling

Authors

Pan, Lehua
Doughty, Christine
Freifeld, Barry

Publication Date

2018

DOI

10.1016/j.geothermics.2017.10.004

Peer reviewed

How to sustain a CO_2-thermosiphon in a partially saturated geothermal reservoir: Lessons learned from field experiment and numerical modeling

Lehua Pan, Christine Doughty, Barry Freifeld

Abstract

CO_2 has been proposed as a working fluid for geothermal energy production because of its ability to establish a self-sustaining CO_2 thermosiphon, taking advantage of the strong temperature dependence of CO_2 density. To test the concept of CO_2 heat extraction, in January 2015 a CO_2 thermosiphon was operated at the SECARB Cranfield Site, Cranfield, Mississippi, where a brine-saturated sand at a depth of 3.2 km has been under near continuous CO_2 flood since December 2009 as part of a U.S. Department of Energy demonstration of CO_2 sequestration, resulting in a partially saturated reservoir surrounding a well pair. The lateral distance between the producer and injector was 112 m at reservoir depth, a distance considered pre-commercial in scale, but great enough that thermal breakthrough was still not significant after several years of injection. Instead of producing power with a turbine, heat was extracted heat from recirculated fluid using a heat exchanger and portable chiller. The well field and surface equipment were instrumented to compare field observations with predicted responses from numerical models. Thermosiphon flow could be initiated by venting, but thereafter flow rate steadily declined, indicating that the thermosiphon was not sustainable. To model the system, the capability of T2Well, a fully coupled wellbore/reservoir numerical simulator, was expanded to enable simulation of the entire loop of fluid circulation in the fully-coupled system consisting of the injection/production wells, the reservoir, and the surface devices (heat exchanger, flow-rate regulator etc.). Combined with the newly developed TOUGH2 equation of state module called EOS7CMA, the enhanced T2Well was used prior to the field experiment to simulate the circulation of a CO_2-H_2O-CH_4 mixture in a model geothermal system patterned after the Cranfield demonstration test. The model predicted that a sustainable thermosiphon could be achieved. After the field thermosiphon did not achieve the pre-test prediction of flow rates and thermosiphon sustainability, the numerical model was modified to improve realism and calibrate certain processes; it was then able to reproduce the major phenomena observed in the field. In a series of sensitivity studies, many factors were found that could potentially contribute to the failing of a sustainable thermosiphon. These factors could be categorized as two types: factors that increase the resistance to flow and factors that increase heat loss of the working fluid. The lessons learned can be applied to both future modeling and to achieving CO_2-based geothermal reservoir exploitation.

Keywords: Sustainability of CO_2-Thermosiphon, Partially saturated reservoir, Field experiment, Coupled wellbore-reservoir-surface devices simulation, T2Well

Nomenclature

A

: Wellbore cross-sectional area m^2

b

: Formation thickness m

C_0

: Shape factor −

C

: Heat capacity J kg^{-1} K^{-1}

g

: Acceleration of gravity vector m s^{-2}

E

: Energy J

F

: Mass flux vector kg m^2 s^{-1}

f

: Apparent friction coefficient −

H

: Enthalpy J

h

: Specific enthalpy J kg^{-1}

k

: Permeability m^2

k_r

: Relative permeability −

m

: Mass kg

n

: Outward unit normal vector −

P

: Total pressure Pa

q_v

Volumetric source term kg m^{-3} s^{-1}

R

Radial coordinate, gas constant m, J kg^{-1} mol^{-1}

S

Saturation, storativity −, m^{-1}

t

Time s

T

Temperature °C

u

Darcy velocity m s^{-1}

u_G, u_L

Phase velocity of gas and liquid in the well m s^{-1}

U

Internal energy J kg^{-1}

v

Velocity m s^{-1}

V

Volume m^3

W

Work J

X

Mass fraction w/phase subscript and component superscript

z

z-coordinate (positive upward) m

Greek symbols

α

Heat exchange coefficient per length of pipe W/°C/m

Γ

Perimeter of wellbore m

γ

Phase interaction term kg m^{-1} s^{-1}

θ

: Angle between wellbore and the vertical °

κ

: Mass components (superscript) −

λ

: Thermal conductivity of fluid-rock composite J m^{-1} s^{-1} K^{-1}

μ

: Dynamic viscosity kg m^{-1} s^{-1}

ρ

: Density kg m^{-3}

τ

: Tortuosity −

ϕ

: Porosity −

Subscripts and superscripts

β

: Phase index

cap

: *capillary*

d

: Drift

G

: Gas

κ

: Component index

l

: Liquid residual

L

: Liquid

m

: Mixture

NK1

Energy component

0

Reference value

r

Relative

R

Rock

res

Bulk reservoir

1. Introduction

Brown (2000) first proposed using CO_2 in place of water as the working fluidfor extracting geothermal heat. Replacing water with CO_2 is hampered by the scarsity of naturally occurring CO_2 sourcesHowever, the widespread adoption of geologic carbon sequestration (GCS), where CO_2 from point sources such as power plants, oil refineries, and ethanol processing facilities is captured and stored underground, will drastically increase the availability of CO_2. Coupling GCS with geothermal energy production can offset some of the incremental costs associated with carbon capture, and end up benefitting both industries (Randolph and Saar, 2011).

The primary benefits cited for using CO_2 as a replacement for water are: (1) its large compressibility and expansivity, which can lead to creation of a natural thermosiphon, wherein CO_2 circulates without the need for external pumping; (2) lower viscosity; and (3) reduced chemical interaction with rock minerals. While CO_2 has a smaller heat capacity than water, when considered in light of its lower viscosity, the greater mobility leads to a net overall increase in efficiency (Pruess, 2006). Pan et al. (2015a) performed coupled wellbore/reservoir numerical simulations to investigate the efficiency of an all-CO_2 system. including heat transfer between the wells and the surrounding formation, and frictional and inertial forces within the wells. However, a more realistic situation is that of a partially saturated reservoir containing both mobile water and CO_2, which complicates the fluid flow process (Pruess, 2006). Under such conditions, the produced fluid may be a mixture of water and CO_2 instead of pure CO_2, which could hurt the performance of the CO_2-based thermal system. For example, the natural thermosiphon, the primary benefit of a CO_2-based system, may not be sustainable because of interference by water in both the well and the reservoir, which could greatly limit the potential for using CO_2 as a working fluid for geothermal energy production. Therefore, the objective of this study is to investigate the sustainability of a thermosiphon in a partially saturated reservoir and identify possible factors that impact sustainability, through a combined approach of field scale experiment and numerical simulations.

The field experiment (Cranfield Test) was conducted at the SECARB Cranfield CFU31 site, the location of a previous U.S. Department of Energy project to demonstrate GCS in a saline aquifer (Hovorka et al., 2013), operated by the South Eastern Regional Partnership for Carbon Sequestration (SECARB). The well site consists of three wells: an injector CFU-31F1 (hereafter referred to as F1) and two collinear observation wells, CFU-31F2 (called F2) about 70 m away, and CFU-31F3 (called F3) another 30 m away at surface. All wells are perforated in the highly heterogeneous, highly permeable, brine-saturated Tuscaloosa sand, which is 3.2 km deep, about 23 m thick, and dips downward at 1–2 ° from F1 toward F3. Ambient pressure is 325 bar and temperature is 129 °C. F1 is the injection well and F3 is used as the production well during the thermosiphon test.

The structure of the paper is as follows. First, the field test and data obtained are summarized. Next the conceptual model and numerical implementation are described, followed by simulation of the experiment results with a calibrated numerical model. Finally, a series of sensitivity studies are performed with the numerical model to reveal the factors that contribute to the sustainability of the thermosiphon in a partially saturated geothermal reservoir, which identifies the shortcomings of the pre-test numerical model.

2. CO_2 Thermosiphon field test

2.1. The site and development of CO_2 filled reservoir

The SECARB Cranfield site (Fig. 1) is the location of a previous project to demonstrate GCS in a saline aquifer. At the time of the thermosiphon test, January 2015, the site had been under near continuous CO_2 flood since December 2009 (Fig. 2), resulting in a partially saturated reservoir surrounding our well pair.

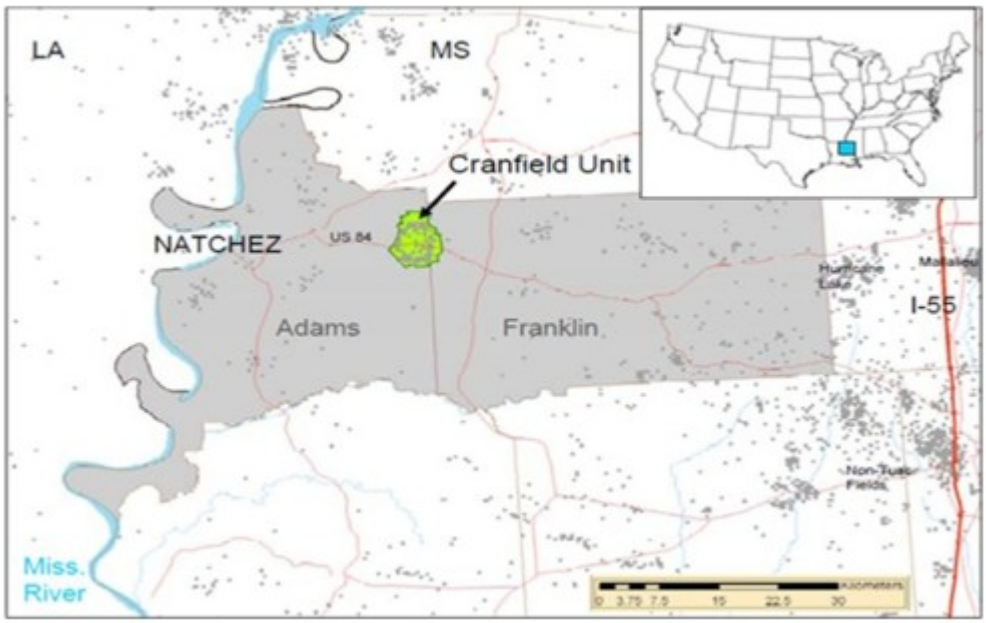

Fig. 1. Location of the Cranfield site at the border of Adams and Franklin County, MS.

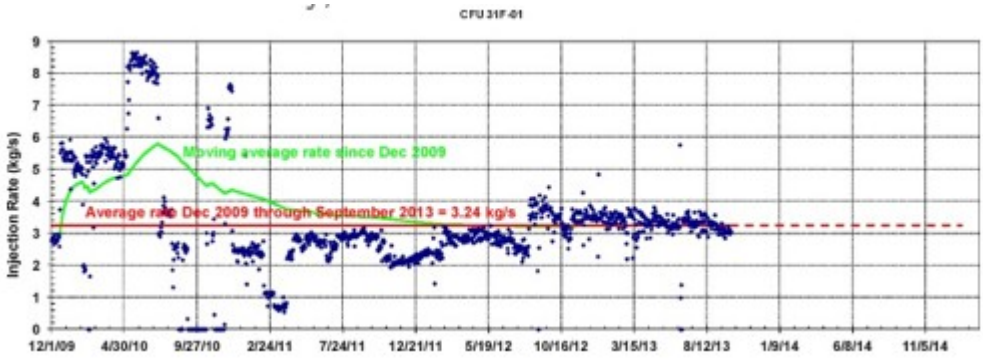

Fig. 2. CO_2 injection rate (blue dots) since December 2009. Green line is the moving average of the flow rate whereas the red line reflects the average flow rate from December 2009 to September 2013, which was used in the numerical model to develop the initial conditions in the reservoir prior to the thermosiphon test.

2.2. Field activities

The Cranfield thermosiphon test utilized well F3 as a producer and well F1 as an injector, operated as a two-well dipole. Data required to calibrate the flow model include well-head pressure and temperature, bottom-hole pressure and temperature, recirculation rate, and fluid density. The upstream and downstream pressure and temperature across the heat exchangers were recorded so as to provide an estimate for the heat extracted by the chiller.

The F3 well was completed with tubing and a packer prior to the initiation of the field trial. In order to record bottom-hole pressure and DTS temperature, a hybrid fiber-optic/copper control line was suspended in the well to simultaneously operate the quartz pressure sensor (Ranger Gauge Systems, Rosharon, TX, USA) and record DTS profiles.

A schematic layout for the surface equipment used during the thermosiphon test is shown in Fig. 3. The surface equipment was installed and commissioned from January 19–21, 2015. The equipment on the schematic in blue is the chilling equipment used to cool the recirculated fluid. The Coriolis flowmeter(Emerson Micro Motion, Colorado, USA, labeled as “Micromotion Flowmeter” in Fig. 3) is able to measure with high accuracy the density of the fluid stream, which can be used to estimate the ratio of CO_2 to brine. Automated valving was installed with the objective of operating in unattended mode with computer supervision. Before and after each critical control point, the pressure (P1 through P4) and temperature (T1 through T4) of the flowing fluid were monitored. Fig. 4 shows the flow iron running between F3 and F1 for the recirculation of the CO_2.

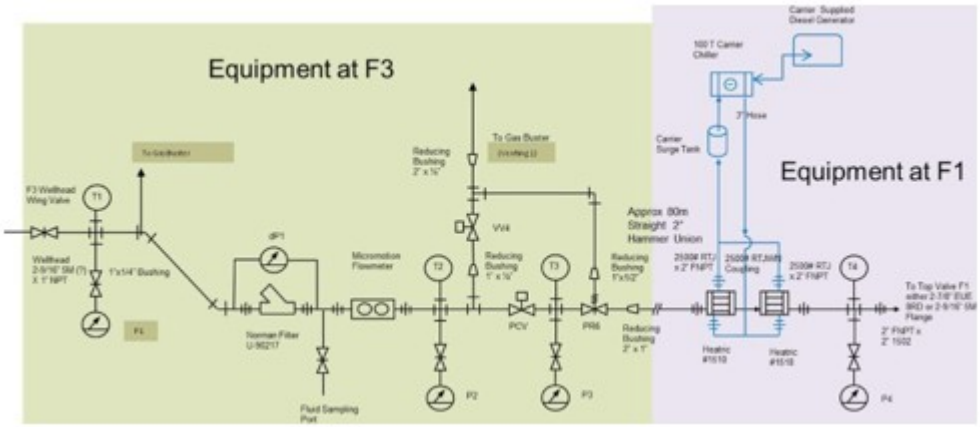

Fig. 3. Sketch of surface equipment and monitoring points. “P1” through “P4” are pressure sensors while “T1” through “T4” are temperature sensors. “PCV” is a valve that can control the flow rate between F3 and F1, including totally shutting off the flow.

Fig. 4. Flow iron looking toward F1 well from F3 well. This is the main recirculation loop for geothermally heated CO_2. The F2 well head appears in the foreground with the more distant F1 well head painted red beyond it.

In order to initiate the thermosiphon, that is, to increase the well-head pressure at F3 such that CO_2 would naturally flow from the F3 production well to the F1 injection well, a vent valve directs the CO_2 from well F3 into a “gas buster” frac tank. When the vent valve is opened, hot CO_2 rapidly moves up the F3 production well. With hotter, less dense fluid in the well, F3 well-head pressure increases. During venting, the flow line to the F1 injection

well is closed, so its pressure does not change. After venting ends, all flow lines are opened and thermosiphon flow from F3 to F1 commences.

Because of several operational issues, such as clogging in various surface devices and formation of CO_2 hydrate, the thermosiphon test was conducted in multiple stages with a number of interruptions. Fig. 5 shows the major stages of the test, while Table 1 provides a brief description of the events. During all siphon periods, flow rate steadily declines, indicating that the thermosiphon is not sustainable.

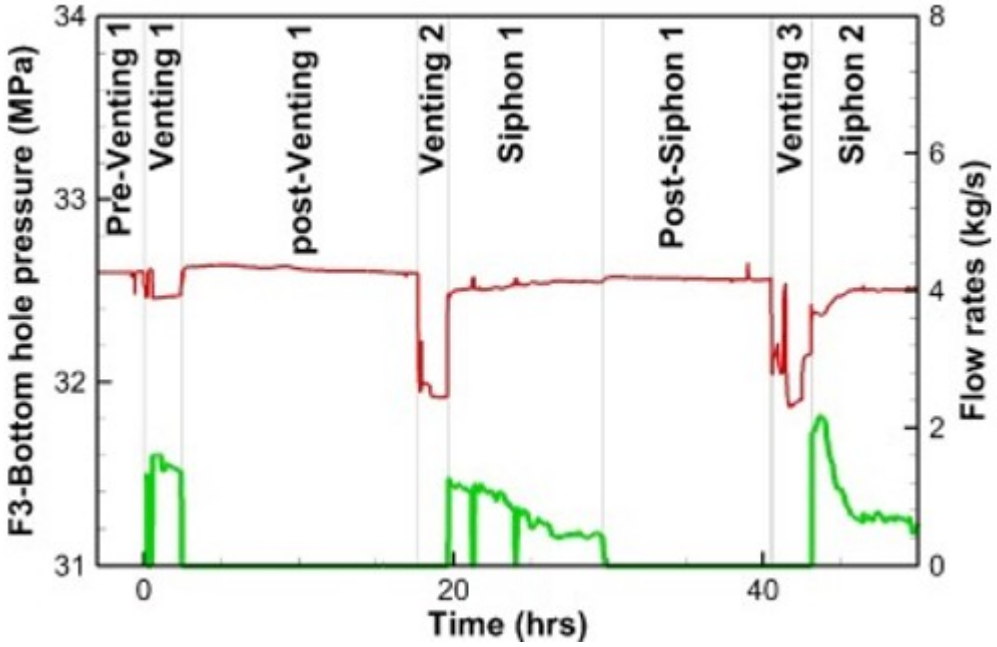

Fig. 5. Major events and associated F3 bottom-hole pressure (red line) and mass flow rate measured by Micromotion Flowmeter (green line). The flow rates during Venting 2 and Venting 3 were not measured because the venting valve was moved in front of the flow meter. The starting point of Venting 1 (01/23/2015 17:48:46) is set as time zero. The events pre-Venting 3 and pre-Siphon 2 are too short to be shown in the figure.

Table 1. List of major events.

Start Time (hr)	**Event**	**Well-head status**		**Note**
		F1	**F3**	
−101.15	pre-Venting 1	open	closed	Injection at F1 with varied rates due to another experiment
0.00	Venting 1	open/ closed	open	Venting after the filter, PCV closed, injection at F1 continued

Start Time (hr)	Event	Well-head status		Note
		F1	F3	
				for about 5.5 h from t = 0 due to another experiment
2.48	post-Venting 1	closed	open	Venting stopped due to filter clog
17.72	Venting 2	closed	open	Venting before the filter, no measurement of flow rate
19.60	Siphon 1	open	open	There was a short shut-in period to clear a clog in the filter
29.62	Post-Siphon 1	open	open	Siphon stopped due to filter clog
39.00	pre-Venting 3	open	closed	External gas introduced to clear the clog in the pipe
40.53	Venting 3	closed	open	Venting before the filter, no measurement of flow rate
42.50	pre-Siphon 2	open	open	Close venting valve to prepare siphon test. PCV valve closed
43.13	Siphon 2	open	open	Siphon ceased at about 87.32 h

3. Conceptual model and grid

The system to be simulated consists of a reservoir, injection well, production well, and surface devices, as shown in Fig. 6.

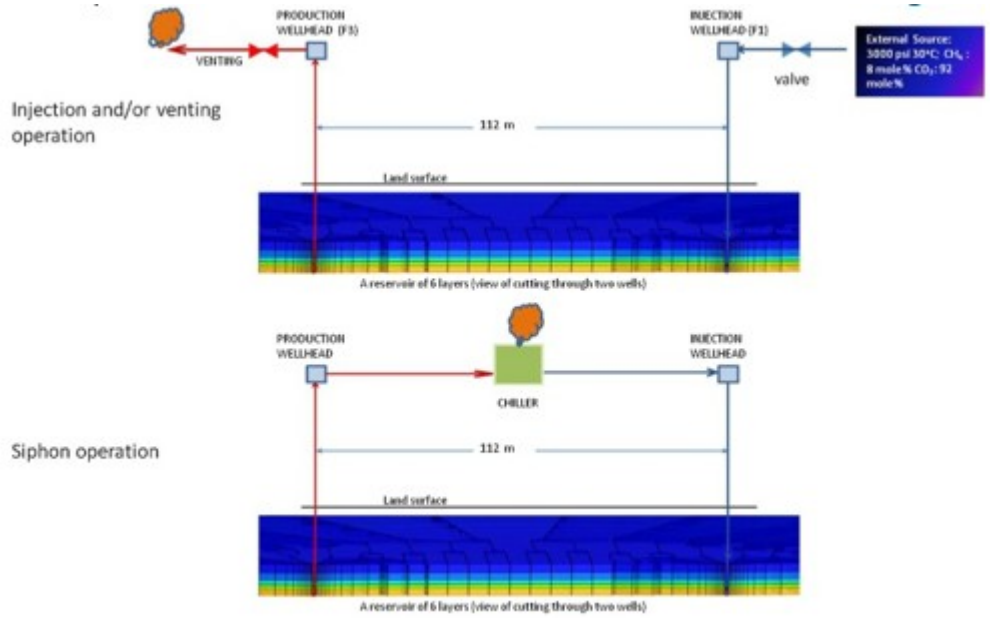

Fig. 6. Sketch of the system at different operational states (not to scale). 1) During initial filling stage (upper panel), gas was transferred from an external pipe into the injection well (F1) while F3 was closed (it was operated as an observation well). 2) During venting stages (upper panel), F3 well head was opened to allow gas to flow while F1 was shut-in. 3) during thermosiphon operation (lower panel), the well head of F3 was connected to the well head of F1 through surface pipes with a chiller in the flow loop to extract heat.

3.1. Reservoir

In the numerical model, the reservoir is horizontal, 23.2 m thick, and located at a depth of 3173.6 m below the land surface. The reservoir consists of six layers with various thicknesses and properties based on well logs from injection well F1 (Hosseini et al., 2013) (e). The reservoir is sandwiched between a low-permeability underlying layer of 30 m thickness and an overlying formation of 3173.6 m thickness. Each of the reservoir layers is uniform except for layers 1, 2, 5, and 6 in which there is a local clay zone embedded in an otherwise uniform sand. A thin skin zone around well F1 (0.17 m) is also assumed to represent permeability reduction due to well completion.

A full three-dimensional (3D) grid with variable lateral resolution was developed to represent a 10 km by 10 km reservoir (Fig. 7a), with the outer boundary located far from the wells to minimize boundary effects. Locally refined grid cells (down to 0.05 m in width) are used in the regions near the injection well and the production well (Fig. 7b). The vertical resolution of the model is the thickness of each layer as shown in Table 2. Fig. 8 shows a cross-section view of the clay zones near production well F3, whereas Fig. 9 shows a map view of the distribution of the clay zones in various reservoir layers. The distribution of the clay zones is designed to qualitatively capture features of the spatial distribution of the CO_2 plume (low saturation in the upper portion of the reservoir near well F3 and in the lower portion of the

reservoir near well F2) that were observed experimentally during the initial filling stage, using electrical resistivity tomography (Carrigan et al., 2013).

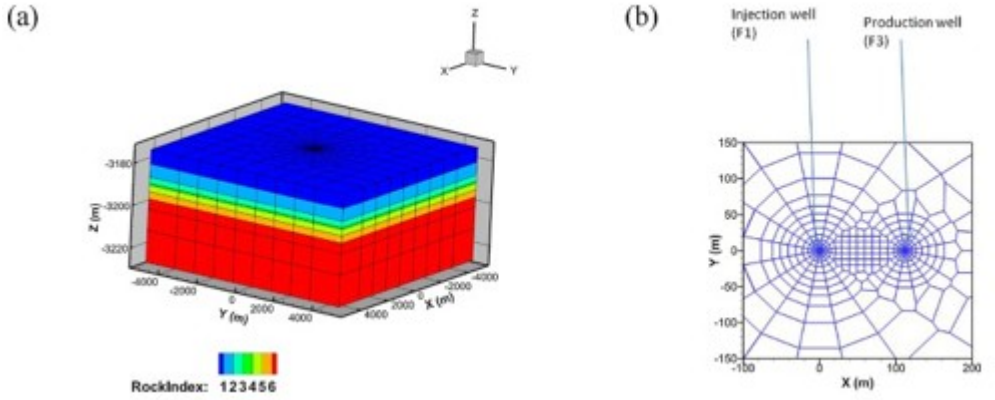

Fig. 7. 3D grid of the reservoir with two wells. Entire 3D mesh (left) and local refinement (right, map view).

Table 2. Formation layers and their properties used in modeling.

Name	Thickness (m)	Porosity	Lateral permeability (× 10^{-15} m^2)	Vertical permeability (× 10^{-15} m^2)	Pore compressibility (Pa^{-1})	Heat conductivity (W/m°C)	Specific heat (J kg^{-1} °C)
Layer1	6.86	0.169	8.60	1.058			
Layer2	6.10	0.254	130.7	47.94			
Layer3	2.90	0.288	230.0	1.32	3.0E-9		
Layer4	0.90	0.139	2.4	0.082			
Layer5	3.00	0.315	349.2	84.87		2.51	
Layer6	3.40	0.283	225.0	0.229			920.0
underlying	30.00	0.083	0.0024	0.000082	0.0		
skins	0.1679 (lateral)	0.139	1.35	0.1058	3.0E-9		
overlying	3173.58	0.139	0.24	0.082		3.50	
clay		0.139	0.10	0.082		2.51	

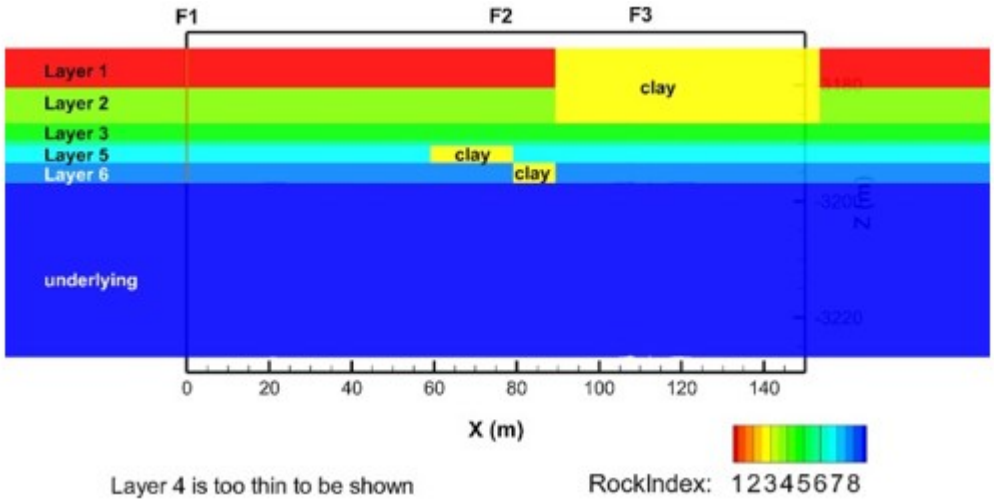

Fig. 8. Cross-section view of the model, illustrating the clay zones.

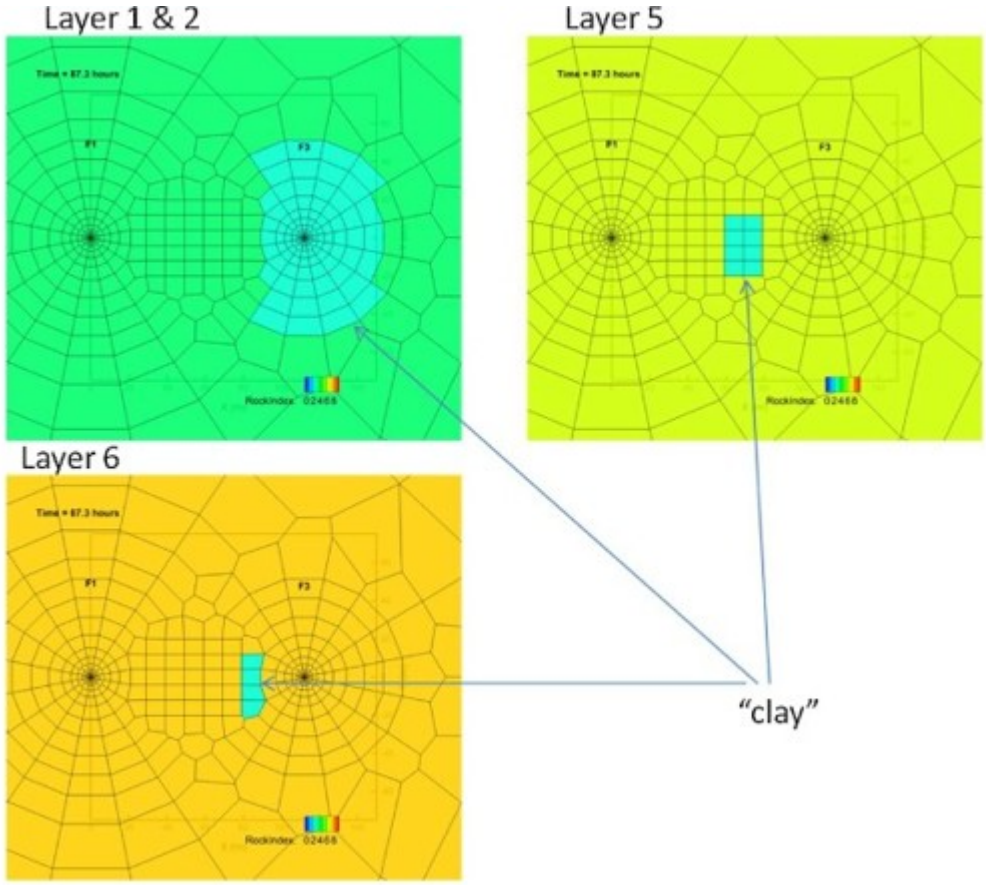

Fig. 9. Map views of the model, showing the distribution of clay zones in various reservoir layers.

The geothermal gradient is assumed to be 35.6 °C/km with T = 127 °C at a depth of 3000 m.

3.2. Wellbores and surface devices

Two wells located in the center region of the simulated reservoir, 112 m apart, are perforated over the high-permeability portion of the reservoir

(Layers 2 through 6) and connected by a pipe at the surface. Table 3 shows the geometry and other parameters of the wellbores and pipe. The inner diameter of the casing (0.1397 m) is used for the width of the wellbore grid cells within the reservoir (below 3173.58 mbgs). Above the top of the reservoir, the inner diameter of the tubing is used for the width of the wellbore grid cells, and representation of the wellbores is simplified such that the tube wall, annulus, and casing are all simulated as part of the surrounding formation. A total of 322 one-dimensionally connected grid cells are used to represent the wellbores above the reservoir and the surface pipe. The vertical resolution of the wellbore grid is 10 m in most places, except that it is gradually reduced to about 3 m near the ground surface, to 4 m near the top of the reservoir, and is the same as that used for the formation layers in the reservoir.

Table 3. Geometry of wellbores and pipes.

Parameter	**Value**
Pipe Length (above ground)	112 (horizontal) + 2 (vertical) m
Well Length (below ground, each)	3196.74 m
Pipe I.D. (connecting two wells at land surface)	2.0 in (0.0508 m)
Tube I.D. (above the reservoir top)	2.4 in (0.06096 m)
Casing I.D. (below the reservoir top)	5.5 in (0.1397 m)
Wall roughness	4.5E-5 (m)
Perforation factor* (F1)	0.2
Perforation factor* (F3)	0.3

* Perforation factor: The effective ratio of the exposed area to the bulk casing surface area, adjusted by the permeabilitycontrast (between exposed rock and the material filling the perforation holes). In actual calibrations, it could also reflect the effects of the local heterogeneity of the formation around wells, which is ignored in the model.

Because the temperature change in the overlying formationwill be limited to a short distance from each well, thermal interference between F1 and F3 through the overlying formation will be negligible. Therefore, axisymmetric grids are used to represent the overlying formation surrounding each of two wellbores, for simulation of conductive heat exchange between the fluid flowing in the wellbore and the overlying formation. The radial outer

boundary of the overlying formation models (at 100 m) can be safely assumed to remain at constant temperature. Numerical simulation is chosen over a semi-analytical solution for modeling the heat exchange between the flowing fluid in the wells and the overlying formation because the semi-analytical solution (Ramey, 1962) used in previous studies (Pan et al., 2015a) is valid only for a system under constant injection or production, which is not the case here. F1 underwent injection of external CO_2 for a prolonged period, then both the injection rate and temperature were transient during this test. F3 was an observation well during the initial filling, then the production rate changed significantly during venting, shut-in, and thermosiphoning. The initial temperature in the overlying formation associated with each well at the start of the filling stage (December 2009, about 5 years before this test) is taken from the natural geothermal gradient.

A large-volume grid cell (fixed temperature of 12 °C) is thermally connected to a section of the pipe between F1 and F3 for simulation of heat exchange between the chiller and the flowing fluid. Another large-volume grid cell (fixed temperature of 6 °C) is thermally connected to all grid cells above the land surface to account for conductive heat transport to the atmosphere.

4. Simulation methods

The simulations are carried out using a modified version of T2Well with EOS7CMA, a research version of the EOS7C code (Oldenburg et al., 2004) that includes air as a pseudo component. T2Well simulates non-isothermal, multiphase, and multicomponent fluid and energy flow in the integrated wellbore/reservoir system, in which the flow in the wellbore is described by the two-phase momentum equation whereas the flow in the reservoir is described by the multiphase Darcy law (Table 4). In this study, three components, H_2O, CO_2, and CH_4, are used. The code has been verified against numerical solutions and field CO_2 production testing data, and has been applied to simulate various scenarios involving coupled wellbore/reservoir flow processes (e.g., Oldenburg and Pan, 2013, Pan and Oldenburg, 2014). The meaning of symbols used in Table 4 can be found in the NOMENCLATURE section.

Table 4. Governing equations solved in T2Well.

Description	**Equation**
Conservation of mass and energy	$\frac{d}{dt}\int_{V_n} M_\kappa dV_n = \int_{\Gamma_n} F_\kappa \cdot n d\Gamma_n + \int_{V_n} q_\kappa dV_n$
Mass accumulation	$M_\kappa = \phi \sum_\beta S_\beta \rho_\beta X_{\beta\kappa}$, for each mass component
Mass flux	$F_\kappa = \sum_\beta X_{\beta\kappa} \rho_\beta u_\beta$, for each mass component

Description		Equation
Porous media	Energy flux	$F_\kappa = -\lambda \nabla T + \sum \beta \rho_\beta u_\beta (h_\beta + gz)$
	Energy accumulation	$M_\kappa = (1-\varphi)\rho_R C_R T + \varphi \sum \beta \rho_\beta S_\beta (U_\beta + gz)$
	Phase velocity	$u_\beta = -k k_{r\beta} \mu_\beta (\nabla P_\beta - \rho_\beta g)$ Darcy's Law
Wellbore	Energy flux	$F_\kappa = -\lambda \nabla T - \sum \beta \rho_\beta S_\beta u_\beta (h_\beta + u_{\beta 22} + gz)$
	Energy accumulation	$M_\kappa = \sum \beta \rho_\beta S_\beta (U_\beta + u_{\beta 22} + gz)$
	Phase velocity	$u_G = C_0 \rho_m \rho_m^* u_m + \rho_L \rho_m^* u_d$ $u_L = (1 - S_{GC0}) \rho_m (1 - S_G) \rho_m^* u_m - S_G \rho_G (1 - S_G) \rho_m^* u_d$ Drift-Flux- Model

To facilitate the simulation of the complete thermosiphon process, the code has been modified by adding additional capabilities for simulating the surface facilities simultaneously with the wellbore and reservoir processes, including the effective pressure drop caused by complicated pipe geometry. Brief descriptions of the approaches and implementations are provided below:

1)

Modeling additional pressure loss caused by complicated flow geometry−

T2Well solves the 1D momentum Eq. (1) to obtain the mixture velocity u_m that will be used to get phase velocities (Pan and Oldenburg, 2014) in wellbore cells. The meaning of symbols used in Eq. (1) can be found in the NOMENCLATURE section.

$$(1)\partial\partial t(\rho_m u_m) + 1A\partial\partial z[A(\rho_m u_m 2 + \gamma)] = -\partial P\partial z - \Gamma f \rho_m |u_m| u_m 2A - \rho_m g \cos\theta$$

Eq. (1) should be practically accurate for a straight, simple-geometry pipe. However, in a system of combined reservoir, wellbores, and surface devices, there are many places where straight pipe flow does not adequately describe the fluid pathway, e.g., the 90° direction change at the tubing/wing-valve connections of both F1 and F3 wellheads, the diameter change between tubing and casing, or the complex geometry inside surface devices such as the condenser (chiller). These features could cause additional pressure loss. To account for this additional pressure loss, the perimeter of the pipe (Γ in

Eq. (1)) is converted into an effective perimeter, which is an input parameter specified for each connection between adjacent wellbore cells. For straight and circular pipe, the effective perimeter Γ is the actual perimeter of the circular pipe cross-section.

1)

Modeling heat exchange in the condenser (chiller) –

The condenser is simulated as a section of surface pipe that is connected to a constant-temperature grid cell through an interface that is impermeable to fluid but has a constant heat exchange coefficient. The conductive heat loss (q_{heat}) through the condenser is calculated as follows:

(2)$qheat=\alpha(Tfluid-Tenvir)$

Where, α is the heat exchange coefficient per length of pipe (2.85×10^5 W/°C/m in this study), T_{fluid} is the fluid temperature, and T_{envir} is a fixed reference temperature (cooling-fluid temperature, 12 °C in this study). Calibrated effective perimeters are also used for pipe/condenser connections to account for the additional pressure loss caused by the condenser and other surface devices.

1)

Modeling flow resistance at the interface between wellbore and formation –

Oilfield perforations are used to connect the region within the casing to the formation. The effective permeability could be very large in these holes but the total cross-sectional area of these holes is only a few percentage of the bulk surface area. In a coupled wellbore/reservoir model, a fine grid (on the order of casing thickness) near the casing/formation interface makes it possible to accurately simulate the flow resistance at that interface. Accurately capturing the flow through the perforations is very important in modeling behavior of the thermosiphon and wellbore/reservoir flow in general. The perforation factor is introduced as an input wellbore parameter (Table 3) to account for the non-ideal perforation effect on the flow. For an ideal perforation, the perforation factor is 1 (the default value), the effective permeability in the calculation of the flow between the well and the formation is exactly the formation permeability just as if the well were an open borehole (i.e., no casing). For other cases, the effective permeability in the calculation of the flow between the well and the formation is the product of the formation permeability and the perforation factor. This approach can also be used for other types of well completion (e.g., screens).

5. Boundary and initial conditions

The reservoir is assumed to be initially saturated with water under a natural geothermal gradient (35.6 °C/km with T = 122.8 °C at a depth of 3005 m) and static pressure (322.8 bar at a depth of 3219.2 m) before initiating CO_2injection in December 2009. Both pressure and temperature at the lower

boundary and far field (5 km away from well F1) are fixed using large-volume grid cells while the top boundary of the reservoir is closed (no fluid or heat flow).

The two axisymmetric overlaying formation domains (one for each well) are also assumed to be initially saturated with water under the same geothermal gradient and hydrostatic pressure. Both pressure and temperature at the top boundary and far field (100 m away from the well) are fixed using large-volume grid cells, while the bottom boundaries of the cap rock domains are closed (no fluid or heat flow).

In the model, well F3 penetrated all the way down into the underlying formation, whereas well F1 only penetrated down through Layer 6. Both wells are perforated in Layers 2 through 6 in the reservoir. For the portion of the well not perforated, only conductive heat flow between the fluid in the well and the surrounding formation is accounted for in the model.

For the surface piping, conductive heat flow between the fluid in the pipe and the atmosphere is simulated assuming atmospheric temperature is fixed at 6 °C, with a calibrated effective thermal conductivity.

Table 5 shows various surface boundary conditions at different stages of the thermosiphon test. During the 5-year initial filling stage, the surface conditions are set similar to the Pre-Venting 1 stage, while the prescribed mass injection rate is 3.24 kg/s (Fig. 2) and the gas composition is 8% (mole) CH_4 and 92% CO_2.

Table 5. Modeled surface boundary conditions.

Time (hr)	**Event**	**Control point status**			
		PCV	**Gas buster**	**Venting Valve**	**External injector**
−101.15	pre-Venting 1	Closed (no flow)	NA	closed	Prescribed mass injection rate
0.00	Venting 1	Closed (no flow)	NA	Prescribed mass production rate	Prescribed mass injection rate
2.48	post-Venting 1	Closed (no flow)	NA	closed	Closed
17.72	Venting	Closed	Fixed	Closed	Closed

Time (hr)	Event	Control point status			
		PCV	Gas buster	Venting Valve	External injector
	2	(no flow)	pressure		
19.60	Siphon 1	open	NA	Closed	Closed
29.62	post-Siphon1	Closed (no flow)	NA	Closed	Closed
39.00	pre-Venting 3	Closed (no flow)	NA	Closed	Prescribed mass injection rate
40.53	Venting 3	Closed (no flow)	Fixed pressure	Closed	Closed
42.50	pre-Siphon3	Closed (no flow)	NA	Closed	Closed
43.13	Siphon 3	open	NA	closed	Closed

6. Results

6.1. Calibration of the model

Prior to simulation of the thermosiphon test, manual calibration exercises were done with a subset of the measured data, to align the model more closely to the real system. The following is a summary.

First, the far-field reservoir pressure and temperature were adjusted, to facilitate matching the measured bottom-hole pressure and temperature at well F3 after the initial filling stage (i.e., during the pre-Venting 1 stage, when no flow occurs). As shown in Fig. 10, the modeled reservoir pressure and temperature are quite close to the measured values. The fitted far-field pressure (not shown here)is higher than hydrostatic pressure, which is attributed to the ongoing far-field CO_2 injection activities within the same dome structure used for tertiary oil recovery.

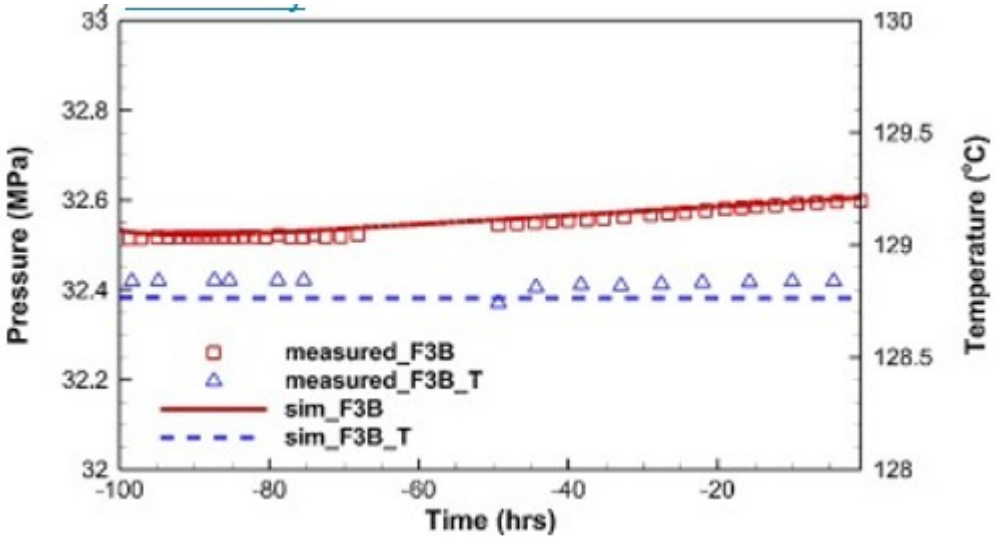

Fig. 10. Comparison of simulated F3 bottom-hole pressure (red solid line) and temperature (blue dash line) against the measured data during the pre-Venting 1 stage. The measurements were made at a depth of 3219.24 m, which is below the perforation zone. (For interpretation of the references to colour in this figure legend, the reader is referred to the web version of this article.)

Secondly, the perforation factor of well F3, the effective perimeters at the F3 tubing/wing-valve connection (where the wellbore tubing connects to surface piping) and the F3 casing-to-tubing reentrant connection at the top of the reservoir, and the effective heat transfer coefficient between the surface pipe and the atmosphere were all adjusted to match the measured temperature T1 (F3 well-head temperature, see Fig. 3) during Venting 1 stage and part of the post-Venting 1 period (Fig. 11). During these stages, the measured mass flow rates through the pipe were specified as the pipe flow rate in the model. As shown in Fig. 11, the temporal variation of T1 is reasonably well reproduced by the numerical model.

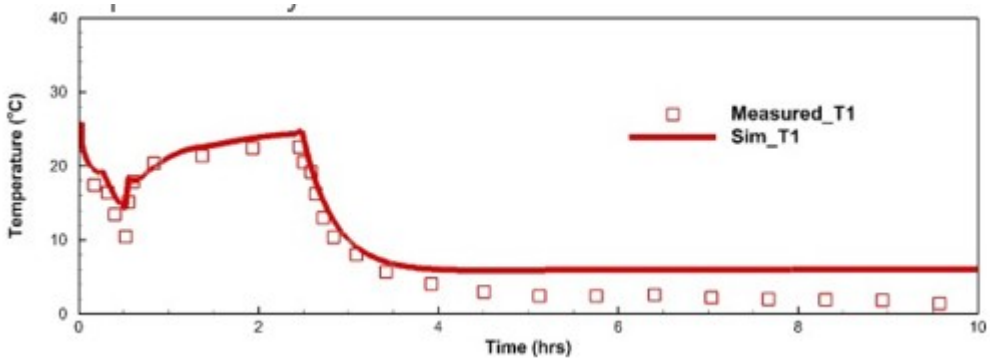

Fig. 11. Comparison of the simulated surface temperature (T1) against the measured values during Venting 1 and post-Venting 1 stages. The actual air temperature dropped to below 0 °C at night but a fixed temperature of 6 °C was used in the simulation for the atmosphere because of a limitation in the simulator's temperature range. As a result, the simulated T1 cannot drop below 6 °C.

Finally, the perforation factor of well F1 and the effective perimeters of the surface condenser, the F1 tubing/wing-valve connection, and the F1 tubing-to-casing reentrant connection at the top of the reservoir were adjusted to match the observed mass-flow-rate dependent pressure losses through

surface devices and the diminishing siphon flow during the Siphon 2 stage (Fig. 12). The Siphon 2 stage was selected as the calibration period because the measured relationship between the pressure drop and the mass flow rate during Siphon 1(red symbols in Fig. 12) was heavily impacted by the formation of CO_2 hydrates in the surface devices. The problem was solved during Siphon 2 as the chiller temperature was raised above the formation point for CO_2hydrate (~12 °C).

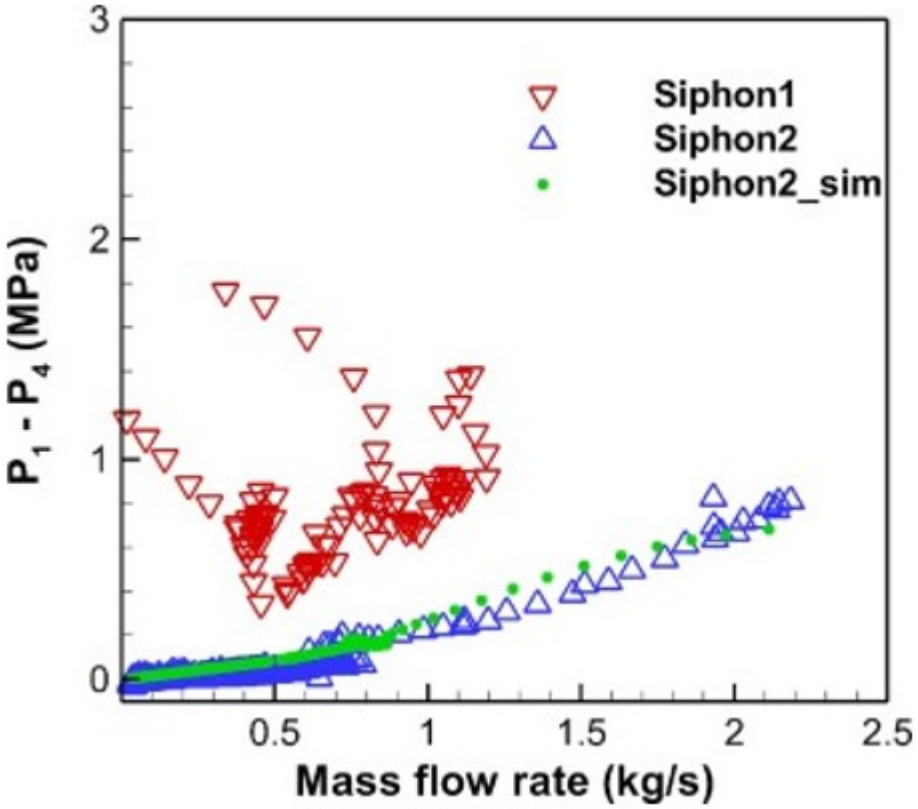

Fig. 12. Simulated and measured pressure difference between surface devices (P1–P4, see Fig. 3) as a function of mass flow rate. Larger variations in the measured data during Siphon 1 are caused by plugging in the filter and other surface devices, a problem that was overcome during the Siphon 2 stage.

6.2. Reservoir status at start of thermosiphon test

After 5 years of injection through well F1 during the initial filling stage, the modeled CO_2 plume extended out to a radius of approximately several hundred meters (Fig. 13a). Because of the low permeability clay zone, the gas saturation around well F3 in the upper portion of the reservoir was very low (Fig. 13b). A cold zone was established around F1 associated with the gas plume, but no significant thermal front reached F3 (Fig. 13d). The injection raised the pressure around F1 in the permeable layers of the reservoir, but the cold plume caused a significant pressure drop in the underlying low permeability layer (Fig. 13c). Fig. 14 provides a detailed view of the reservoir conditions in the F1–F3 cross section. Well F3 has limited connectivity to the CO_2 plume (Layers 3, 5, and 6), with the lower portion of

the reservoir (below Layer 4) serving as the major channel for communication between F1 and F3. The relationships between the clay zones and wells can be seen more clearly in map-view plots of liquid saturation in the major layers (Fig. 15).

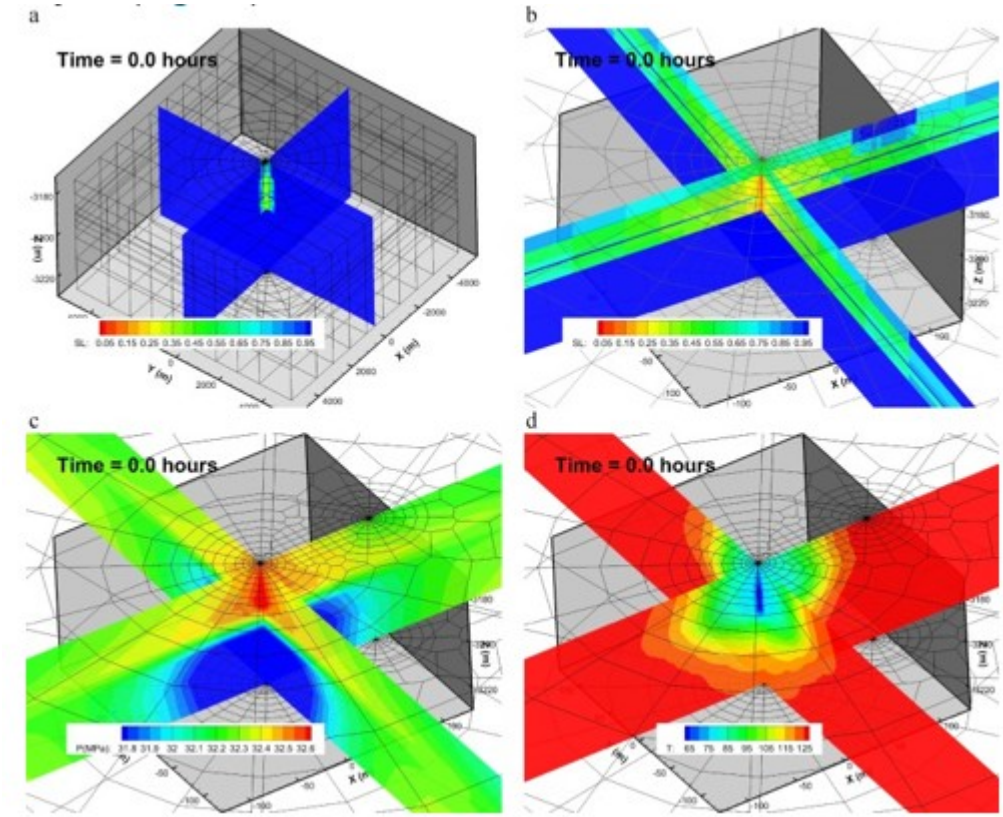

Fig. 13. Simulated reservoir conditions at start of thermosiphon test, defined as time = 0. (a) liquid saturation in entire domain, (b) liquid saturation in the F1–F3 region, (c) pressure in the F1–F3 region, and (d) temperature in the F1–F3 region. F1 is located at the center of the bigger circular grid while F3 is located at the center of the smaller circular grid on the right of the plots.

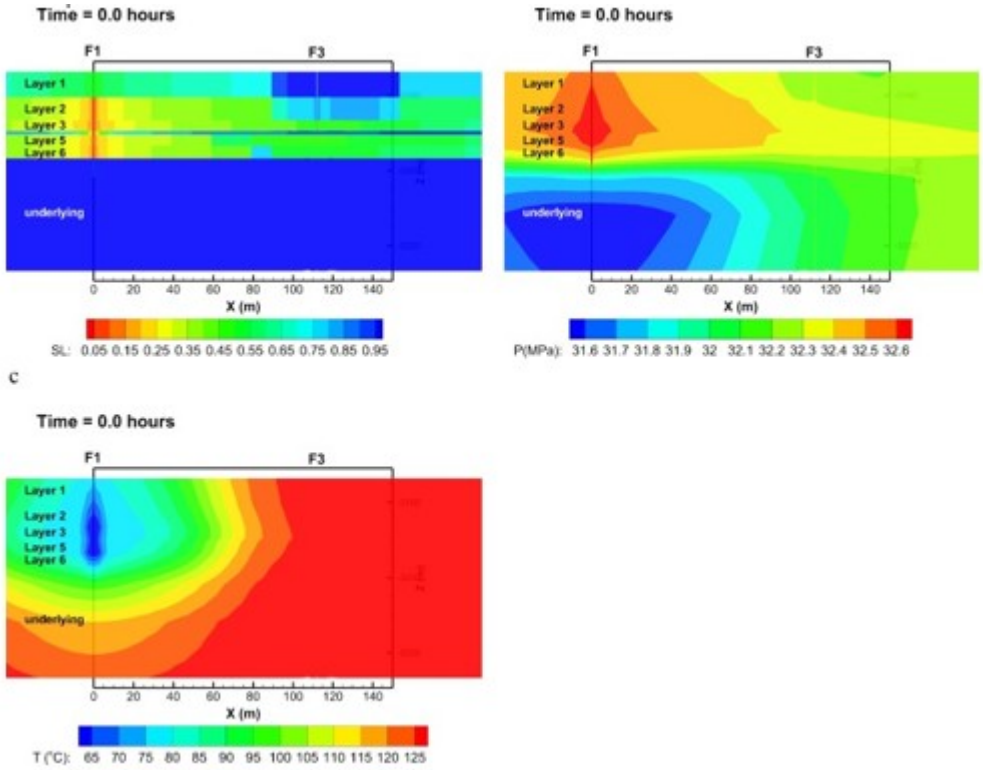

Fig. 14. F1–F3 cross-section view of (a) liquid saturation, (b) pressure, and (c) temperature at start of thermosiphon test. Well F1 is located at x = 0 m whereas well F3 is located at x = 112 m. Note that liquid saturation plot is not interpolated, but is shown with a uniform color block for each grid cell.

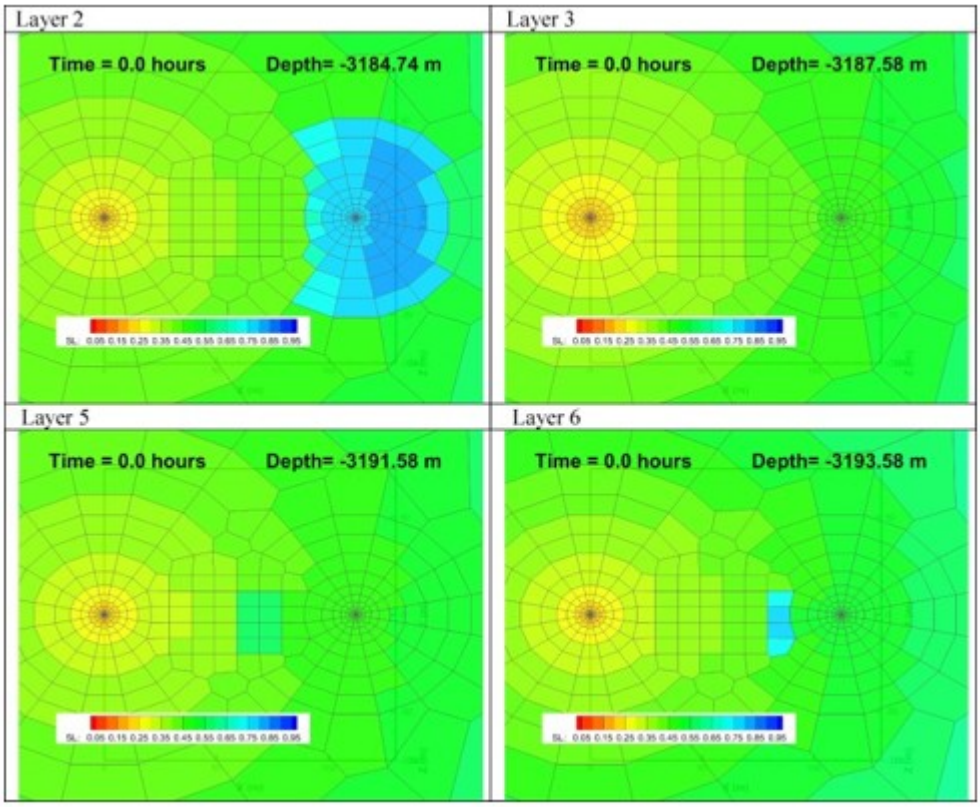

Fig. 15. Liquid saturation in major layers (map view) at start of test. The clay zones show up as local high liquid saturation regions. Well F1 is located at the center of the circular grid on the left side while Well F3 is on right side.

6.3. Thermosiphon test

The calibrated model was used to simulate the entire thermosiphon testing sequence. Fig. 16 shows the simulated mass flow rate during different stages of the test against the measured data. As mentioned before, the measured mass flow rate data during Venting 1 were specified for the model, whereas the flow rate during Venting 2 and 3 could not be measured because the venting valve was installed before the flow meter. The model captures the major trend of the siphon flow: diminishing with time. Because of the formation of hydrate in surface equipment, Siphon 1 prematurely ended at 19.5 h, and the measured mass flow rate decreases faster than predicted by the model, which does not take into consideration hydrate formation. During Siphon 2 the model is able to predict the diminishing siphon flow reasonably well except for early time when the venting transitions to thermosiphoning. This might be because the real system has a stronger thermal buffer than the model, which keeps the production well warmer for a longer time than in the simulation.

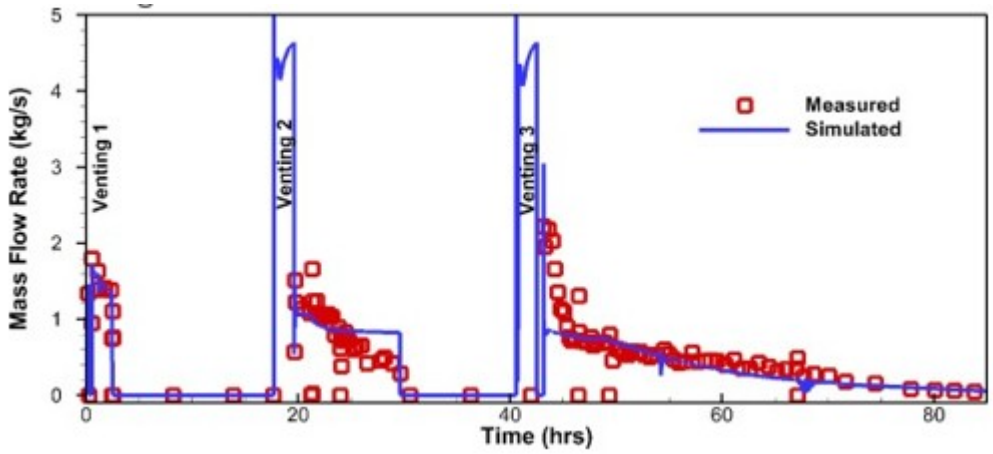

Fig. 16. Comparison of simulated mass flow rate against the measured values. The flow rate was not measured during Venting 2 & 3 stages because the venting valve was installed before the flow meter.

As shown in Fig. 17 (upper panel), although the model overpredicts the drop of T1 during early times after the initiation of thermosiphoning, the model reproduces the major variations in temperature during various test stages. Similarly, the model reproduces the pressure responses to the test events reasonably well (Fig. 17, lower panel) except from 30 to 40 h, when the recirculation was halted due to clogging after Siphon 1. It is unclear why measured P1 did not fall off as predicted (Fig. 17, lower panel). The large measured pressure difference between P1 and P4 during Siphon 1 (20–30 h) is believed to be caused by clogging in the surface devices that is not included in the model. The pressure jumps before Venting 3 are caused by introduction of external pressurized gas used to purge the surface devices and pipe. Because of a lack of detailed information of this operation (pre-

Venting 3), in the model it is simplified as an injection event with a guessed flow rate that ended before Venting 3. Furthermore, the model also reproduces the F3 bottom-hole pressure and temperature (Fig. 18). Because the sensors are located below the well perforations, where the well is always saturated with water (higher heat capacity fluid), the response in temperature to various stages in the test is very small, although the pressure drops quickly in response to venting events. The overall F3 bottom-hole pressure decreases with time after the thermosiphon test starts, reflecting the net volumetric production of fluids from the reservoir, since the warm CO_2 that is produced is less dense than the cool CO_2 that is injected.

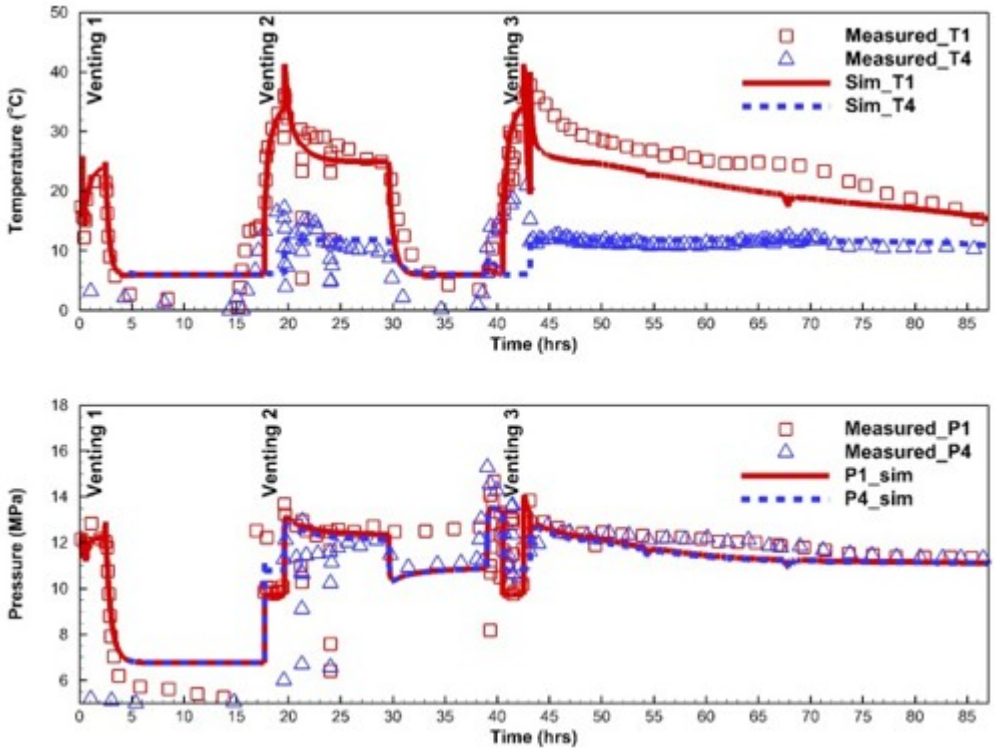

Fig. 17. simulated and measured temperatures T1 and T4 (upper panel) and presures P1 and P4 (lower panel).

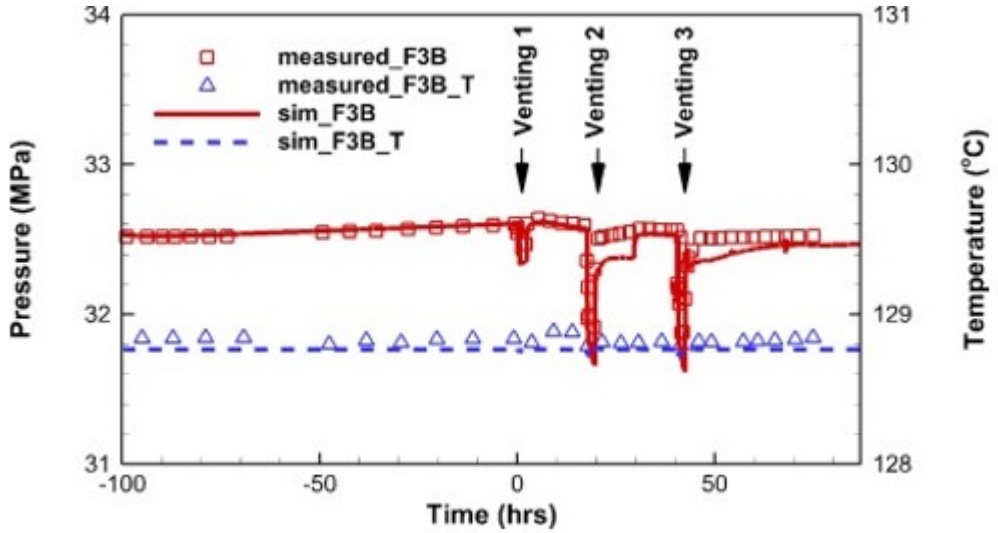

Fig. 18. Simulated and measured F3 bottom-hole temperature (blue) and pressure (red).

Fig. 19 shows the temperature profiles in wells F3 and F1 changing with time. Venting quickly raises the temperature in the production well (F3), but the temperature quickly drops as the flow rate is reduced (e.g., siphon started or shut in). In the injection well (F1), the overall temperature trend is increasing, due to greater warming of CO_2 from the overlying formation, because the average downward flow rate is smaller than that prior to the thermosiphon test (3.24 kg/s).

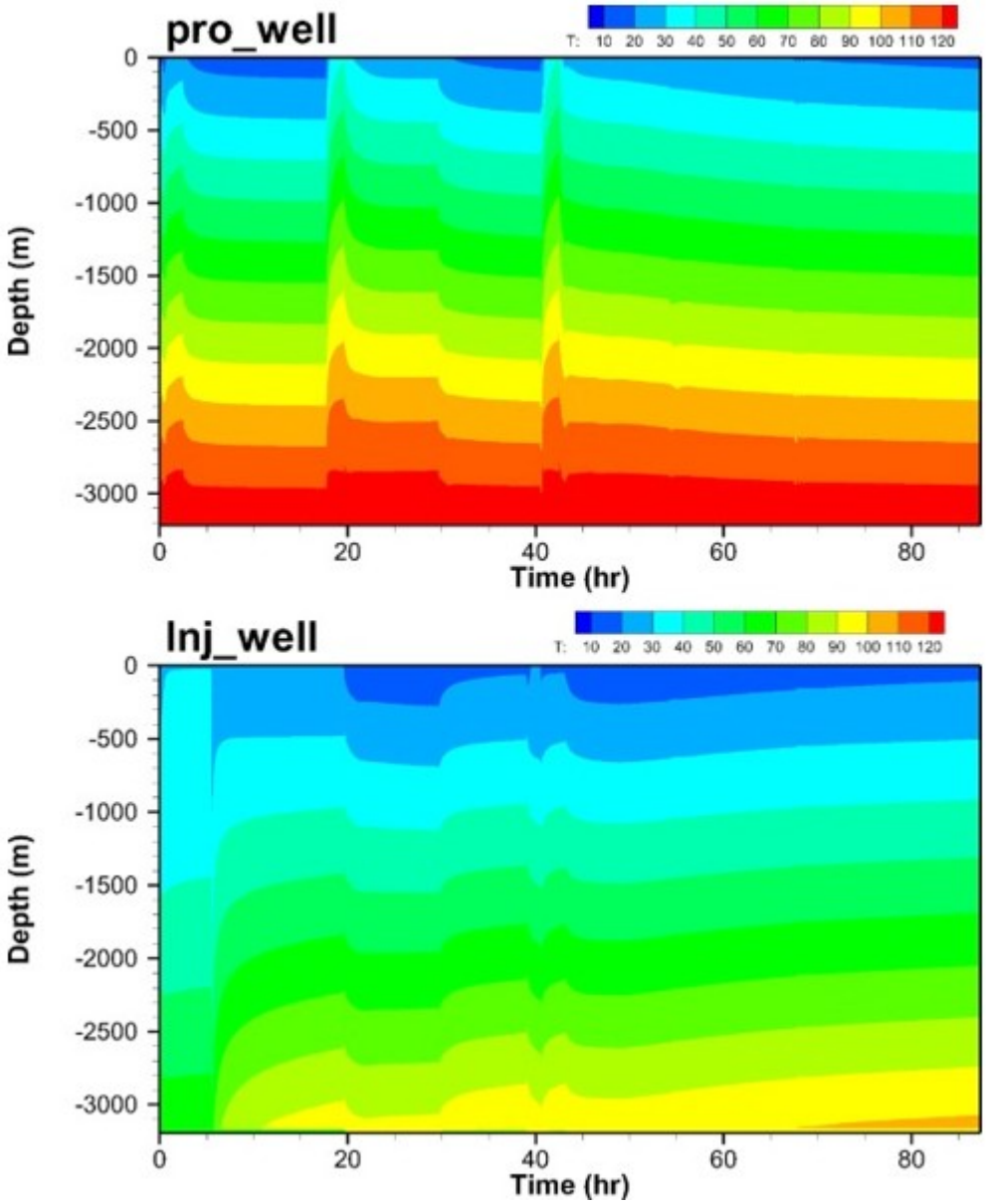

Fig. 19. Simulated temperature profiles in the production well (F3, upper panel) and the injection well (F1, lower panel) over time. Venting (during 0.00–2.48, 17.72–19.60, and 40.52–42.50 h) quickly raises temperature in the production well.

As shown in Fig. 20, venting increases moisture in the production well (F3) because higher velocity gas can carry more liquid water. The liquid saturation in the production well becomes smaller after the thermosiphon starts (at 19.60 or 43.13 h) because the lower velocity gas transports less water. However, as temperature further drops, condensate water starts to counterflow back down the well resulting in a two-phase region forming during the latter portion of each siphon period. This phenomenon can be seem most clearly during Siphon 2 (43.13–87.00 h) with water accumulating in the bottom of the well and some water temporarily (hours 45–55) found in the middle of the well (Fig. 20, upper panel). The complexity of multiphase

counter-flow is difficult to fully capture in a numerical model, but field observations showed widely varying rates of liquid production, with slugs of water circulating through the surface piping. This produced water was recirculated back down the injection well.

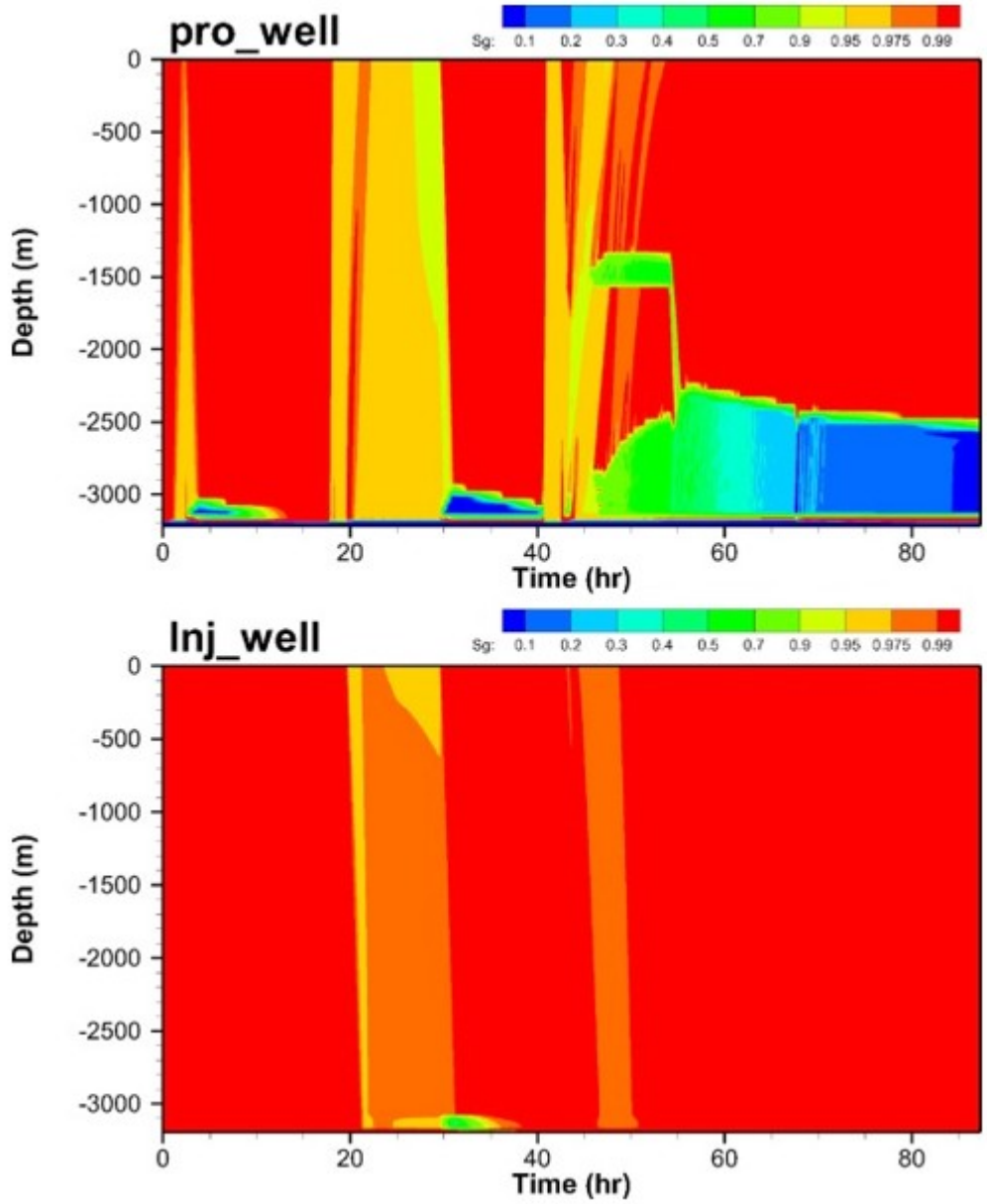

Fig. 20. Simulated gas saturation profiles in the production well (F3, upper panel) and the injection well (F1, lower panel) over time (venting occurs during 0.00–2.48, 17.72–19.60, and 40.52–42.50 h). Note that a refined scale is used for gas saturation above 0.9.

As shown in Fig. 21, the gas density in the production well is lower than that in the injection well, and this difference in gas density is the driving force for thermosiphon flow. Furthermore, enough mass flow rate is needed to cancel the effects of heat loss in the production well and heat gain in the injection well so that the density difference between the production and injection

wells can be maintained at a high level to sustain the siphon flow. As shown in Fig. 21, the overall trend of gas density is increasing in the production well and decreasing in the injection well although venting temporally interrupts such trends. As a result, the thermosiphon flow diminishes over time.

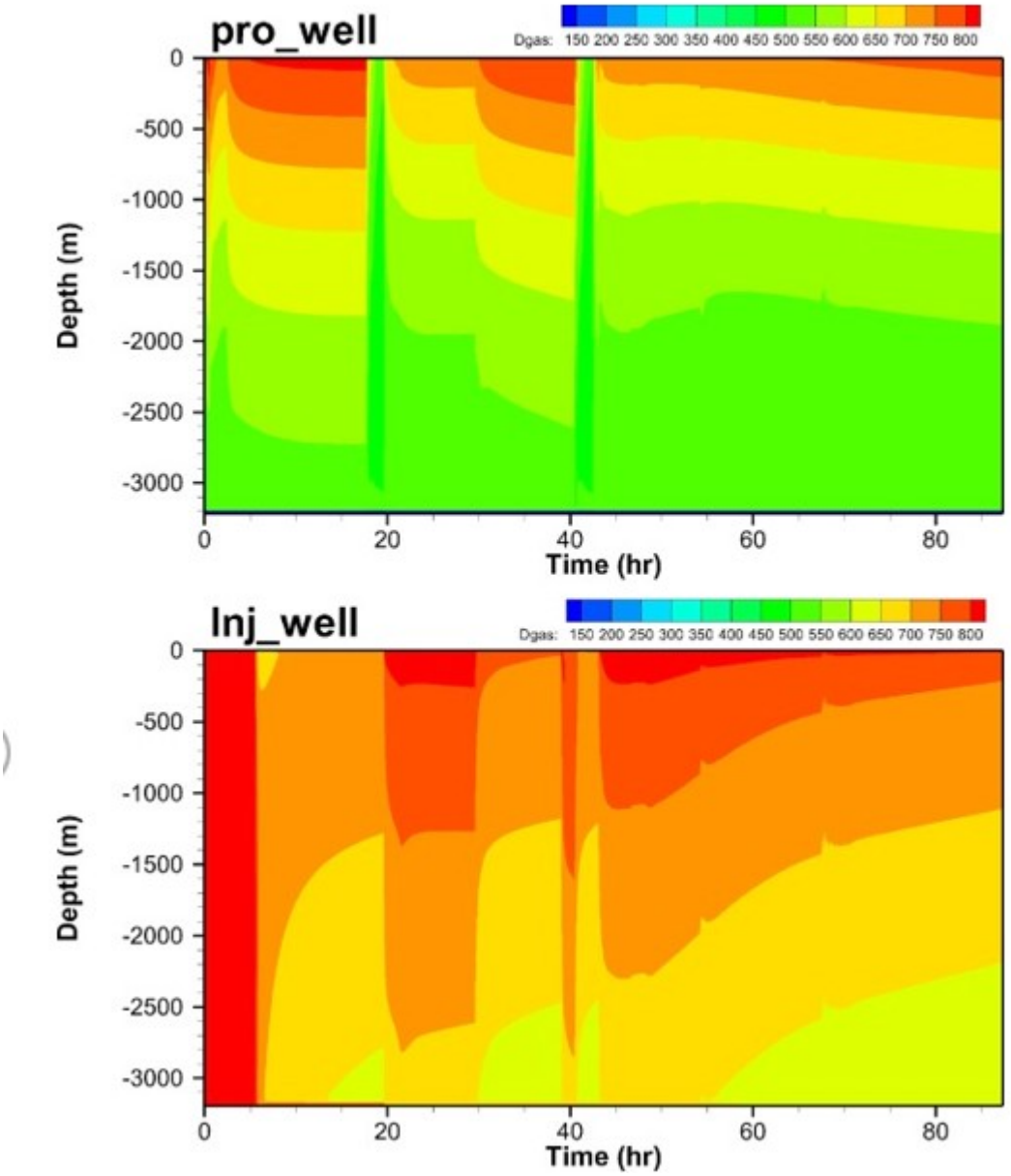

Fig. 21. Simulated gas density profiles in the production well (F3, upper panel) and the injection well (F1, lower panel) over time (venting occurs during 0.00–2.48, 17.72–19.60, and 40.52–42.50 h).

6.4. Effects of various factors on thermosiphon

To identify factors that could impact the sustainability of a thermosiphon, a series of numerical experiments were done, based on a variety of conceptual reservoir models for the Cranfield site. To simplify the analysis, instead of the complicated multiple stages of the real field test, the test process was

considered to occur in two stages: 2 h of venting followed by 72 h of recirculating. The initial conditions are created as a result of 5 years of injection at 3.24 kg/s.

- Homogeneous Case: effects of clay lens

The Homogeneous Case deviates from the base case by removing the clay lenses in Layers 1, 2, 5, and 6. As a result, each layer is homogenous. Such changes in the geological model would affect the distribution of the CO_2 plume after the initial 5 years of injection. Therefore, the initial conditions before the siphon test are recalculated with new geology. It is observed that by merely removing the clay heterogeneity, there are profound impacts on the predicted behavior of the thermosiphon. Fig. 22 shows that the Homogeneous Case results in an increase in produced fluid temperatures and higher flow rates as compared to the Base Case. The removal of the clay lens near well F3 increases gas saturation around F3 (Fig. 22d, compared to Fig. 14a) and provides more pressure support from the injection in well F1. As a result, the system is able to sustain a siphon flow (Fig. 22a) mainly because of the contribution of inflow from Layer 2 under the same pressure gradient. Although the sustained flow rate is small, it seems to be just above the minimum flow rate that keeps the production well-head temperature high enough to maintain the siphon flow against the competing heat loss into the surrounding formation. As the heat loss decreases with time due to a decrease in the temperature gradient between fluid in the well and the surrounding formation (Fig. 22b), both T1 and mass flow rate increase with time. During the 2 h period of venting (simulated as a process with fixed F3 well-head pressure), the simulated mass flow rate is slightly higher in the Homogeneous case than in the Base case (Fig. 22a), reflecting the additional resistance to flow caused by the clay lens around F3. In other words, a stronger pressure gradient is needed in the Base Case than in the Homogeneous Case. It is observed that early in the operation of the thermosiphon, when the mass flow rate and well-head temperature are almost identical in both cases (Fig. 22a & b), the pressure difference between the wells (P1 and P4) is already greater in the Homogeneous Case (Fig. 22c). It is this pressure difference that controls the fate of the thermosiphon, resulting in the sustainability of the Homogenous Case and the decline in the Base Case.

- Insulated Case: the effects of tubing insulation

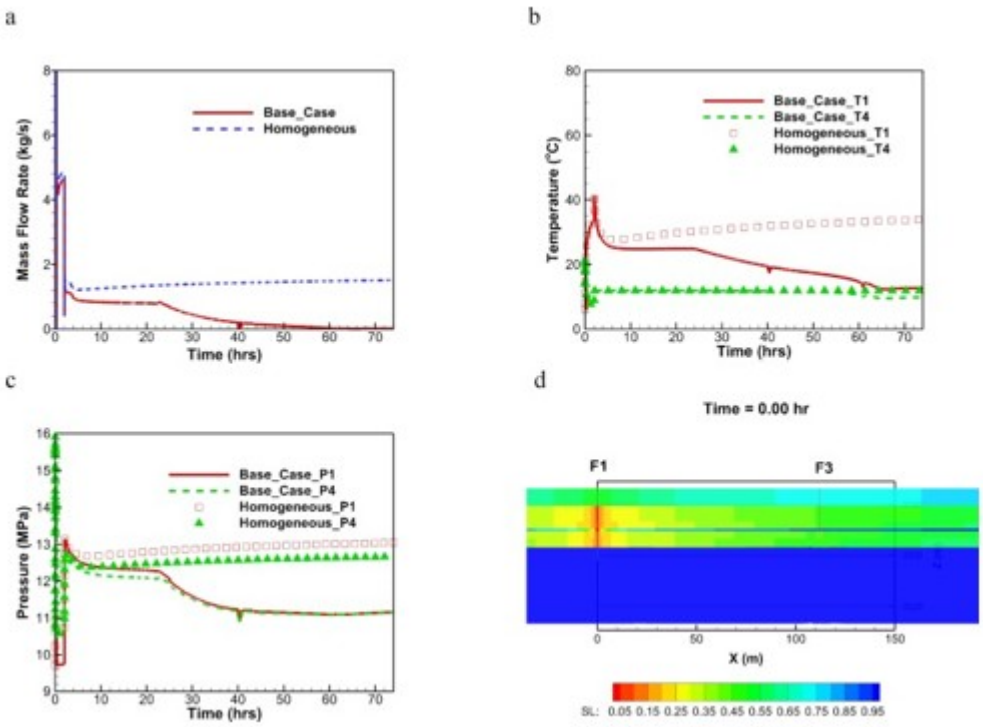

Fig. 22. Effects of clay zones on thermosiphon. (a) mass flow rate, (b) surface temperature T1 and T4, (c) surface pressure P1 and P4, and (d) Homogeneous Case initial liquid saturation before venting. “Base_Case” −with clay zones; “Homogeneous” −without clay zones.

Heat exchange between the flowing fluid and the surrounding formation through the tubing wall occurs in two different directions in the system. In the production well (F3), the fluid loses heat to the surrounding formation because it is warmer than the surroundings. In the injection well (F1), on the other hand, the fluid gains heat from the surrounding formation because it is colder than the surroundings. Such heat exchange is harmful to thermosiphon flow. There are two practical ways to achieve a reduction in heat exchange through the tubing wall: (1) through the use of dual-wall production tubing that is insulated, or (2) through the replacement of the fluid in the annulus with a gas or supercritical fluid such as CO_2 that has a very low thermal conductivity. In the numerical model, such insulation can be simulated by simply reducing the tubing wall heat conductivity, regardless of the actual physical approach adopted. As a result, in the Insulated Case, tubing wall heat conductivity is 0.03 W/mK (compared to 2.51 W/mK in the Base Case). Everything else is the same as in the Base Case. Fig. 23 shows the comparisons of the simulated results between the Insulated Case and the Base Case. The reduced heat exchange results in warmer fluid in F3 and colder fluid in F1, which makes thermosiphon flow sustainable at a level of about 2 kg/s (Fig. 23a). Because of insulation, little heat would be lost to the surrounding formation. As a result, the F3 well-head temperature (T1) can quickly approach 80 °C and remain at that level (Fig. 23b). For a similar reason, the F1 bottom-hole temperature in the insulated case quickly reduces to below 40 °C as compared to above 80 °C in the base

case (Fig. 23d). The warmer gas in F3 results in higher well-head pressure (P1) in the insulated case which makes higher siphon flow possible (Fig. 23c). The F1 (injection) well-head pressure is also higher in the insulated case which is needed to drive the gas down at the higher flow rate.

- High T Case: effects of higher geothermal gradient

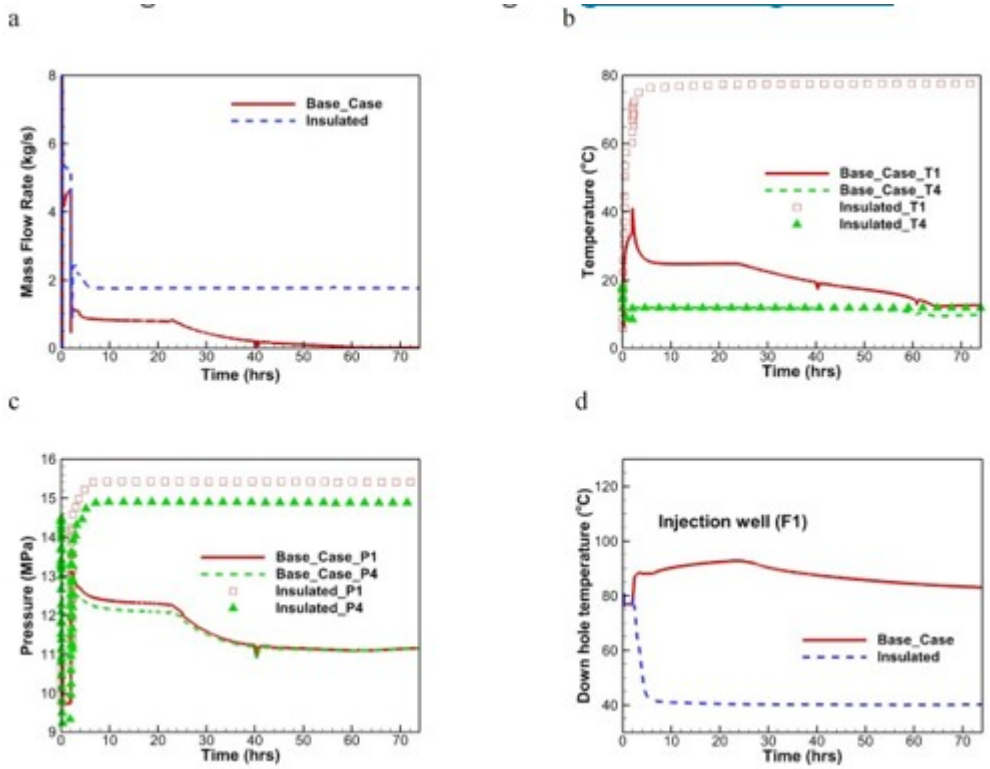

Fig. 23. Effects of insulation of tubing on thermosiphon. (a) mass flow rate, (b) surface temperature T1 and T4, (c) surface pressure P1 and P4, and (d) down hole temperature in F1. “Basecase” −wall heat conductivity = 2.51; “Insulated” −wall heat conductivity = 0.03.

While the temperature at the Cranfield Site is considered as below optimal for EGS, the readily available infrastructure of the site offered a compelling reason for its selection. A region with higher geothermal gradient would be of great interest because it would lead to higher potential for heat extraction as well as improve the sustainability of a thermosiphon. To this end, the High T Case is designed, which deviates from the base case by using a higher geothermal gradient (51n°C/km instead of 35.6 °C/km). The resulting reservoir temperature is about 177 °C instead of 127 °C. Because the geothermal conditions are changed, the initial conditions before the siphon test are recalculated for the High T Case. Fig. 24 shows comparison of the simulated results between the High T Case and the Base Case. A higher reservoir temperature provides more heat for the same fluid mass, which reduces relative effects of heat loss to surrounding formation and in turn the system can sustain a higher thermosiphon flow rate (Fig. 24a). The F3 well-head temperature (T1) quickly increases above 40 °C and gradually

increases with time as a result of decreasing of heat loss to the surrounding formation (Fig. 24b). A similar trend is found in terms of well-head pressure (Fig. 24c). However, hotter formations also increase the heat gain in the injection well (F1) which results in much higher bottom-hole temperature than the base case (Fig. 24d). As a result, higher injection pressure is needed to drive this lighter gas down in F1 (Fig. 24c). As the heat exchange rate between flowing fluid in the wells and the surrounding formation decreases with time, the flow rate slowly increases to reflect the diminishing of the heat exchange effects (Fig. 24a).

- Ideal Pipe Case: effects of geometry changes and perforation effectiveness

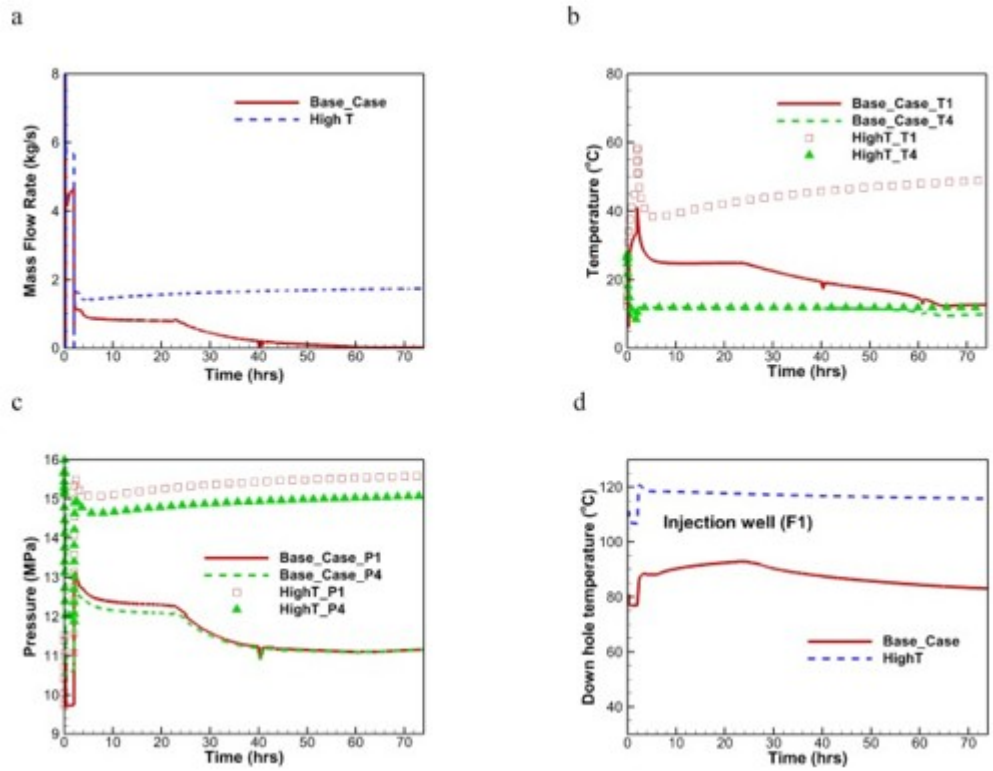

Fig. 24. Effects of geothermal gradient on thermosiphon. (a) mass flow rate, (b) surface temperature T1 and T4, (c) surface pressure P1 and P4, and (d) down hole temperature in F1. “Basecase” −35.6 °C/km; “High T” −51.0 °C/km.

Resistance caused by geometry changes in the wellbores and surface devices as well as head loss across perforations play a big role in determining the sustainability of the thermosiphon because it greatly reduces deliverability for the same thermodynamic conditions. In the Ideal Pipe Case, the perforation factor is set to 1 (i.e., perfect) and all the additional pressure drops caused by geometry changes (e.g., jointer, elbow, and other non-circular and non-straight shapes) in the system were removed. As shown in Fig. 25a, the siphon flow rate could be above 4 kg/s,

which is the highest of all cases considered. The reason is that the pressure gradient that is needed to drive the circulation is much smaller in this “ideal pipe” system (Fig. 25c) even though T1 is just above 40 °C, slightly higher than the High T case and about half that of the Insulated Case (Fig. 25b). The F1 bottom-hole temperature is only slightly lower than the base case because of the high flow rate. The results imply that reducing resistance to flow in the entire system, including improving deliverability across the perforations, reducing sudden size changes, and smoothing the flow path in the surface devices is important to maintaining a thermosiphon. Since it will never be realistic to eliminate all of these flow restrictions, properly considering these factors in the model is critical to generating more realistic prediction and avoiding overly optimistic predictions, as was done in pre-test modeling (Pan et al., 2015b).

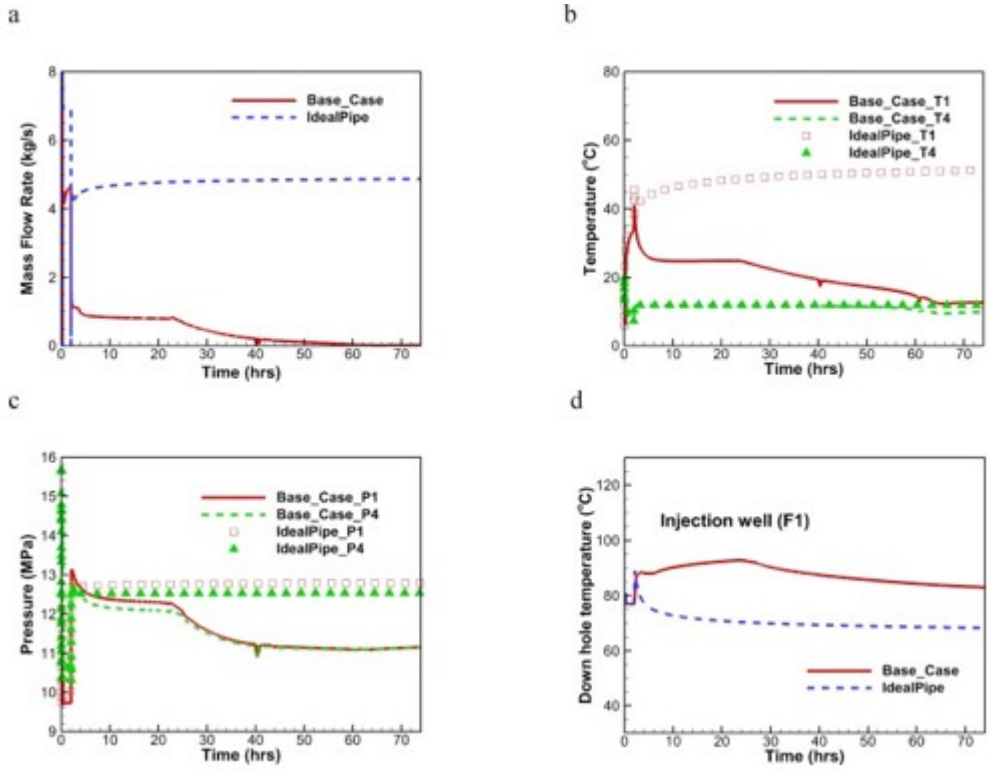

Fig. 25. Effects of resistance caused by changing geometry and imperfect perforation on thermosiphon. (a) mass flow rate, (b) surface temperature T1 and T4, (c) surface pressure P1 and P4, and (d) down hole temperature in F1.

The key results for the Base Case and all the alternate cases are summarized in Fig. 26. The Base Case cannot sustain a thermosiphon, as shown in Fig. 26a. If the clay lens that impedes the flow in the reservoir in the Base Case is removed (Homogeneous Case), the system sustains the thermosiphon flow above 1.2 kg/s. In this case, the flow rate first decreases immediately after venting to about 1.2 kg/s and then gradually increases with time as the heat loss in F3 and heat gain in F1 is gradually reduced. If the reservoir is hotter (High T case), more heat is carried by the produced fluid, which makes the system more tolerant of heat loss to the formation and thus maintains

sufficient mass flow rate. However, the fluid in the injection well is also hotter (so lighter) which impedes the system's ability to maintain a higher thermosiphon flow rate. Cutting the heat exchange between wellbores and surrounding formation (Insulated Case) plays a big role in maintaining the thermosiphon, because it makes the fluid in F3 warmer (so lighter) and F1 colder (so heavier). Not observed in the other cases, we note the flow rate in the Insulated Case is almost constant because the temporal change in heat exchange between fluid in the production (or the injection) tubing and the formation is much less important in the Insulated Case. The resistance in the flow path has a large effect on the sustainable thermosiphon flow (Ideal Pipe Case) indicating the positive feedback between the thermosiphon flow and the thermosiphon driving force that maintains flow. Although eliminating flow resistance is not realistic, this case indicates the potential to improve the performance of the system by paying careful attention to the perforation density selected and reducing other piping related head losses in the system.

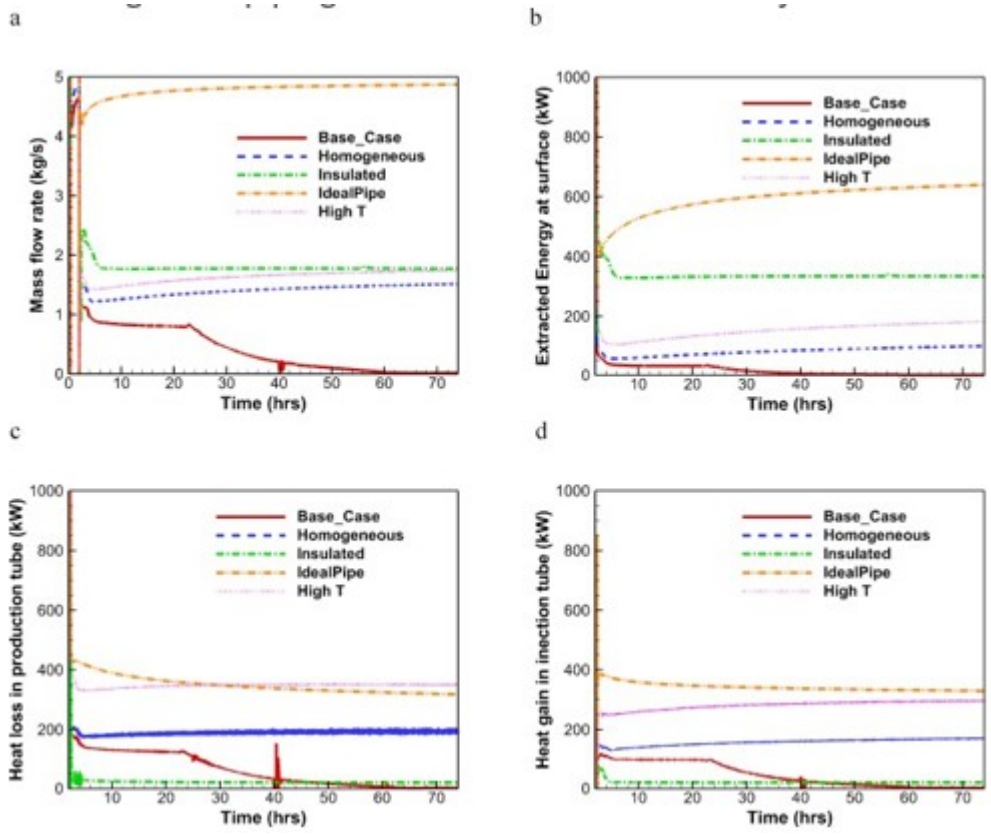

Fig. 26. simulated mass and heat flow rate during thermosiphon in different cases. (a) mass flow rate, (b) heat extracted at surface, (c) heat loss in production tubing (F3 above packer), and (d) heat gain in injection tubing (F1 above packer).

Heat loss in production tubing and gain in injection tubing are usually proportional to the mass flow rate for the same geothermal gradient except for the Insulated Case (Fig. 26a, c, d). A higher geothermal gradient results in higher heat loss in the production tubing and higher heat gain in the

injection tubing. As a result, the energy extracted at the surface in the High T case is much lower than in the Insulated Case (Fig. 26b) even though the flow rate is only slightly lower than in the latter (Fig. 26a).

7. Conclusions

The first field scale experiment for producing geothermal energy by recirculating CO_2 between a well pair was performed. The experimental results show that after initiating a pressure gradient between the producer and injectorby venting the producer at a high flow rate, thermosiphon flow decreases with time until it is no longer self-sustaining. To interpret the field observations, a new capability for simulating the entire flow loop was developed, including injection/production wells, the reservoir, and surface pipes and devices. A modified version of the T2Well/EOS7CMA code was used to model the transport of $H_2OCO_2CH_4$ throughout the coupled reservoir/well/surface piping system.

The model, after it had been manually calibrated against a subset of the data obtained in the Cranfield demonstration experiment, can reproduce most of the important features observed in the field experiment reasonably well, including those periods when the observed data were not used in the calibration.

A series of simulations was then performed, to understand this result and what changes could be made to improve the outcome of the experiment. The Homogeneous Case and the Ideal Pipe Case examine effects of decreasing the resistance to flow and the High T Case and the Insulated Case illustrate the impact of decreasing heat loss of the working fluid, two factors that strongly impact the sustainability of a thermosiphon.

The Base Case numerical experiment shows that the clay lenses around production well F3 in the upper portion of reservoir and between F1 and F3 in the lower portion of the reservoir limit access to well F3 of the CO_2 plume and increases the resistance to flow through the reservoir. If these barriers did not exist, the Homogeneous Case suggests the thermosiphon flow could be sustainable, although at a low rate of about 1.2 kg/s.

The pressure drop attributed to piping restrictions and other surface devices, as well as limited deliverability of the perforations, is found to play a big role in the sustainability of a thermosiphon. If these flow restrictions were removed (Ideal Pipe Case), the siphon flow rate could be maintained above 4.5 kg/s (the highest value of all investigated cases). Although ideal pipe and perfect perforations are not realistic, efforts to reduce these resistances to flow are extremely important in developing a thermosiphon. Meanwhile, accurately modeling flow restrictions is critical to obtaining an accurate prediction.

The High T Case showed that increasing the reservoir temperature about 50 °C could result in a sustainable thermosiphon flow at a higher rate (>1.5 kg/s). The hotter fluid entering the production well could tolerate the heat

loss to the formation to keep the production well warm and result in higher production well-head temperature, resulting in more thermal energy available for extraction at surface. On the other hand, a hotter formation could heat the fluid in the injection well more effectively and result in a warmer injection well, which is not favorable for maintaining the thermosiphon.

The Insulated Case in which both the tubing in the production and injection well have a low thermal conductivity to the formation is found to be very helpful in sustaining thermosiphon flow. If the tubing is insulated, the thermosiphon flow could be sustained at the same (or slightly higher) rate as that of the High T case. Insulation of the tubing also greatly enhances the system performance in terms of y extraction at the surface.

While this experiment should be viewed as only the first step in demonstrating the use of CO_2 as a heat mining fluid, the lessons that learned are invaluable in design and planning of subsequent experiments.

Acknowledgment

This work was funded by the Assistant Secretary for Energy Efficiency and Renewable Energy, Geothermal Technologies Program of the U.S. Department of Energy under Contract No. DE-AC02-05CH11231. We wish to thank Kirk DeLaune from Sandia National Laboratory for his assistance in conducting the field work. Field operations were supported by Paul Cook, Alejandro Morales, Alex Sun, Jiemin Lu, Kate Hart, Jim Underschultz and Melody Xiuhui Li.

References

Brown, 2000

D.W. Brown**A hot dry rock geothermal energy concept utilizing supercritical CO_2 instead of water**

Proceedings of the Twenty-fifth Workshop on Geothermal Reservoir Engineering, Stanford University, CA, USA, (pp. 233–238) (2000)

Carrigan et al., 2013

C.R. Carrigan, X. Yang, D.J. LaBrecque, D. Larsen, D. Freeman, A.L.Ramirez, W. Daily, R. Aines, R. Newmark, S.J. Friedmann, S. Hovorka**Electrical resistance tomographic monitoring of CO_2 movement in deep geologic reservoirs**

Int. J. Greenh. Gas Control, 18 (2013), pp. 401-408

Hosseini et al., 2013

S.A. Hosseini, H. Lashgari, J.W. Choi, J.-P. Nicot, J. Lu, S.D. Hovorka**Static and dynamic reservoir modeling for geological CO_2 sequestration at Cranfield, Mississippi, U.S.A**

Int. J. Greenh. Gas Control, 18 (2013), pp. 449-462

Hovorka et al., 2013

S.D. Hovorka, T.A. Meckel, R.H. Trevino**Monitoring a large-volume injection at Cranfield, Mississippi – project design and recommendations**

Int. J. Greenh. Gas Control, 18 (2013), pp. 345-360

Oldenburg and Pan, 2013

C.M. Oldenburg, L. Pan**Porous media compressed-air energy storage (PM-CAES): theory and simulation of the coupled wellbore–reservoir system**

Transp. Porous Media, 97 (2) (2013), pp. 201-221

LBNL-6529E

Oldenburg et al., 2004

Oldenburg, C.M., G.J., Moridis, N., Spycher, K., Pruess, EOS7C Version 1.0: TOUGH2 module for carbon dioxide or nitrogen in natural gas (methane) reservoirs, Lawrence Berkeley National Laboratory Report LBNL-56589, March 2004.

Pan and Oldenburg, 2014

L. Pan, C.M. Oldenburg**T2Well—an integrated wellbore-reservoir simulator**

Comput. Geosci., 65 (2014), pp. 46-55

Pan et al., 2015a

L. Pan, B. Freifeld, C. Doughty, S. Zakem, M. Sheu, B. Cutright, T. Terrall**Fully coupled wellbore-reservoir modeling of geothermal heat extraction using CO_2 as the working fluid**

Geothermics, 53 (2015), pp. 100-113

Pan et al., 2015b

L. Pan, C. Doughty, B. Freifeld, C.M. Oldenburg**Modeling a CO_2 thermosiphon in a partially saturated reservoir using EOS7CMA**

Proceedings, TOUGH Symposium 2015, Lawrence Berkeley National Laboratory, Berkeley, CA, September 28–30 (2015)

Pruess, 2006

K. Pruess**Enhanced geothermal systems (EGS) using CO_2 as working fluid—a novel approach for generating renewable energy with simultaneous sequestration of carbon**

Geothermics, 35 (4) (2006), pp. 351-367

Ramey, 1962

H.J. Ramey Jr.**Wellbore heat transmission**

J. Petrol. Technol., 225 (1962), pp. 427-435

Randolph and Saar, 2011

J.B. Randolph, M.O. Saar**Combining geothermal energy capture with geologic carbon dioxide sequestration**

Geophys. Res. Lett., 38 (10) (2011)